Angewandte Chemie
Eine Zeitschrift der Gesellschaft Deutscher Chemiker

Supporting Information

Zeolite-Encaged Pd–Mn Nanocatalysts for CO_2 Hydrogenation and Formic Acid Dehydrogenation

Qiming Sun, Benjamin W. J. Chen, Ning Wang, Qian He, Albert Chang, Chia-Min Yang, Hiroyuki Asakura, Tsunehiro Tanaka, Max J. Hülsey, Chi-Hwa Wang, Jihong Yu, and Ning Yan**

ange_202008962_sm_miscellaneous_information.pdf

Methods

Chemical and materials. Tetrapropylammonium hydroxide solution (TPAOH, 1M, SIGMA-ALDRICH PTE LTD); tetraethylorthosilicate (TEOS, SIGMA-ALDRICH PTE LTD); Manganese (II) chloride tetrahydrate ($MnCl_2 \cdot 4H_2O$, Sinopharm Chemical Reagent CO. LTD, ≥ 99%); Palladium chloride ($PdCl_2$, Pd≥59%, SIGMA-ALDRICH PTE LTD); Tetraethylenepentamine ($(NH_2CH_2CH_2NHCH_2CH_2)_2NH$, SIGMA-ALDRICH PTE LTD, ≥ 99%); Ethylenediamine ($NH_2CH_2CH_2NH_2$, ≥99%, SIGMA-ALDRICH PTE LTD); Deionized water from Millipore (Milli-Q, 18.2 MΩ/cm; Millipore, Bedford, MA); Triethylamine ($N(CH_3CH_2)_3$, SIGMA-ALDRICH PTE LTD); Sodium carbonate (Na_2CO_3, Aldrich); Sodium carbonate ($NaHCO_3$, SIGMA-ALDRICH PTE LTD, ≥99.7%); Sodium hydroxide (NaOH, SIGMA-ALDRICH PTE LTD); Formic acid (FA, HCOOH, 98%, Aladdin); Pd/C catalyst (5 wt.%, SIGMA-ALDRICH PTE LTD); Pd/Al_2O_3 catalyst (1 wt.%, SIGMA-ALDRICH PTE LTD).

Preparation of $[Pd(NH_2CH_2CH_2NH_2)_2]Cl_2$ and $[Mn(NH_2CH_2CH_2NHCH_2CH_2)_2NH]Cl_2$ precursor solutions. The $[Pd(NH_2CH_2CH_2NH_2)_2]Cl_2$ solution (0.18 M) was prepared by dissolving 0.32 g of $PdCl_2$ into 10 mL of an aqueous solution containing 2 mL of ethylenediamine under stirring until becoming a clear solution. The $[Mn(NH_2CH_2CH_2NHCH_2CH_2)_2NH]Cl_2$ (0.18 M) solution was prepared by dissolving 0.37 g of $MnCl_2 \cdot 4H_2O$ into 10 mL of an aqueous solution containing 1 mL of tetraethylenepentamine under stirring until becoming clear solution.

Synthesis of Pd@S-1 catalyst. Pd@S-1 catalyst was synthesized with the molar composition of 1.0 SiO_2: 0.4 TPAOH: 35 H_2O: 0.0045 $[Pd(NH_2CH_2CH_2NH_2)_2]Cl_2$ under hydrothermal conditions at 170 °C for 3 days.

Typically, the mixture was prepared by first mixing the deionized water with 16.25 g TPAOH solution (1 M), followed by continuous stirring for 10 min. 8.32 g TEOS was then added into the above mixture. After continuous stirring for 6 h, the synthetic solution became clear. Following, 1 mL of $[Pd(NH_2CH_2CH_2NH_2)_2]Cl_2$ solution was added into the above mixture and further stirred for 30 min. Finally, the reaction mixture was transferred into a 100 mL Teflon-lined stainless steel autoclave and the crystallization was conducted in a conventional oven at 170 °C for 3 days under static conditions. The as-synthesized solid product was centrifuged, washed with water several times,

and then dried in a vacuum freeze drier for 24 h, followed by calcination in air at 550 °C for 6 h. Finally, the sample was reduced by H_2 at 400 °C.

Synthesis of $PdMn_x$@S-1 catalysts with different Pd/Mn molar ratios. $PdMn_x$@S-1 catalysts (x = 0.2, 0.4, 0.6, and 0.8, respectively. x represents different Pd/Mn molar ratios) were synthesized with the molar composition of 1.0 SiO_2: 0.4 TPAOH: 35 H_2O: 0.0045$[Pd(NH_2CH_2CH_2NH_2)_2]Cl_2$: x$[Mn(NH_2CH_2CH_2NHCH_2CH_2)_2NH]Cl_2$ (x = 0.0009, 0.0018, 0.0027, 0.0036) under the similar conditions to Pd@S-1, respectively.

Typically, the mixture was prepared by first mixing the deionized water with a 16.25 g TPAOH solution, followed by continuous stirring for 10 min. 8.32 g TEOS was then added into the above mixture. After continuous stirring for 6 h, the synthetic solution became clear. Following, 1 mL of $[Pd(NH_2CH_2CH_2NH_2)_2]Cl_2$ and 0.2 ~ 0.8 mL of $[Mn(NH_2CH_2CH_2NHCH_2CH_2)_2NH]Cl_2$ solution was added into the above mixture and further stirred for 30 min. Note that the $[Mn(NH_2CH_2CH_2NHCH_2CH_2)_2NH]Cl_2$ precursor solution needs to be used immediately after the preparation, otherwise the $[Mn(NH_2CH_2CH_2NHCH_2CH_2)_2NH]Cl_2$ precursor solution will precipitate soon. However, interestingly, when the $[Mn(NH_2CH_2CH_2NHCH_2CH_2)_2NH]Cl_2$ solution was added to the above synthesis gel, the precipitation can not be observed, indicating this complex are stable in the synthesis gel during the synthetic procedure. Finally, the reaction mixture was transferred into a 100 mL Teflon-lined stainless steel autoclave and the crystallization was conducted in a conventional oven at 170 ℃ for 3 days under static conditions. The as-synthesized solid product was centrifuged, washed with water several times, and then dried in a vacuum freeze drier for 24 h, followed by calcination in air at 550 °C for 6 h. Finally, the sample was reduced by H_2 at 400 °C.

Synthesis of Mn@S-1 catalyst. Mn@S-1 catalyst was synthesized with the molar composition of 1.0 SiO_2: 0.4 TPAOH: 35 H_2O: 0.0045 $Mn(NH_2CH_2CH_2NHCH_2CH_2)_2NH]Cl_2$ under the similar conditions to $PdMn_x$@S-1, excepting without adding the $Pd(NH_2CH_2CH_2NH_2)_2]Cl_2$ solution.

Synthesis of silicalite-1 (S-1) zeolite. The synthesis procedure of S-1 zeolite is similar to that of Pd@S-1, except without adding the metal complex.

Synthesis of Pd/S-1-im catalyst. Pd/S-1-im catalyst was prepared by the incipient wetness impregnation method. Typically, 1 g of silicalite-1 zeolite (the template has been removed by calcination in air at 550 °C) was first impregnated with 0.3 mL 0.2 M $(NH_4)_2PdCl_4$ solution. The

resulting solid was dried in a vacuum freeze drier for 24 h and then reduced in flowing H_2 at 400 ℃ for 2 h.

Characterization. The crystallinity and phase purity of the samples were characterized by powder X-ray diffraction (PXRD) on a Rigaku D/Max 2550 diffractometer using Cu Kα radiation (λ = 1.5418 Å). The transmission electron microscopy (TEM) images, mapping images, and corresponding energy dispersive X-ray (EDX) spectrometry were measured with a Tecnai F20 electron microscope. Aberration-corrected scanning transmission electron microscopy (STEM) high angle annular dark-field (HAADF) images were taken at 200 kV on a JEOL ARM-200CF microscope. Inductively coupled plasma (ICP) analyses were carried out on an iCAP 7600 ICP-OES instrument. Nitrogen adsorption/desorption measurements were carried out on a Micromeritics 3 Flex Physisorption Analyzer at 77.35 K after the samples were degassed at 350 °C under vacuum. Thermogravimetric and differential thermal analyses (TG-DTA) were carried out on a NETZSCH STA 449C in the air at a heating rate of 10 °C min^{-1} from room temperature to 800 °C. The metal dispersions of samples were determined by H_2 chemisorption measurements that were carried out in a Micromeritics AutoChem II 2920 automated chemisorption analysis unit. ^{13}C MAS NMR spectra were performed on a Bruker AVANCE III 400 WB spectrometer at resonance frequencies of 100.6 MHz with a spinning rate of 8 kHz. X-ray photoelectron spectroscopy (XPS) was performed using an ESCALAB 250 spectrometer. Pd K-edge X-ray absorption spectra (XAS) of supported catalysts and references (Pd foil and PdO) were recorded at the BL01B1 beamline at the Spring-8 (Japan Synchrotron Radiation Research Institute, Hyogo, Japan), and Mn K-edge XAS of the catalysts and references (Mn foil, MnO, Mn_2O_3, and MnO_2) were measured at the beamline BL17C1 at National Synchrotron Radiation Research Center (NSRRC), Taiwan.

CO_2 and H_2 were analyzed using Agilent GC 6890N, equipped with thermal conductivity detector (TCD) and Plot-Q column (Agilent J&W GC Columns, HP-PLOT/Q 19095P-Q04, 30m × 530μm × 40μm). Detailed analyses for CO were performed on GC-7806 with flame ionization detector (FID)-Methanator (detection limit: ~10 ppm). The formates product was analyzed using high-performance liquid chromatography (SHIMADZU, DGU-20A) equipped with Hi-plex H column (300 × 7.7 mm) and RID detector.

In situ diffuse reflectance infrared Fourier transformed spectra (DRIFTS). In situ DRIFTS experiments were performed on a Nicolet iS50 FT-IR spectrometer equipped with a high

temperature DRIFTS reaction cell (Harrick Scientific Products, INC) using an MCT/A detector in the series mode with 32 ~ 256 scans and at a resolution of 4 cm^{-1}.

In situ DRIFTS of CO adsorption experiments, 50 mg as-synthesized sample (after calcination in air and reduction in H_2) was first activated in pure H_2 flow (25 mL/min) at 573 K (with linear heating to 573 K for 1 h and holding for 1 h). Following, the gas flow was switched to pure N_2 (40 mL/min) for 0.5 h until the system was cooled down to room temperature. After taking the background spectrum under N_2 atmosphere at room temperature, 5% CO balance with Ar (50 mL/min) was admitted for 1 h until saturated and then purged with N_2 (30 mL/min). The DRIFTS spectra were recorded during the N_2 purge.

In situ DRIFTS of CO_2 + H_2 experiments, the catalyst (50 mg) was first activated in pure H_2 flow (25 mL/min) at 573 K (with linear heating to 573 K for 1 h and holding for 1 h). Following, the gas flow was switched to pure N_2 (40 mL/min) for 0.5 h until the system was cooled down to 373 K. After taking the background spectrum under the N_2 atmosphere at 373 K, the gas flow was switched into a mixture of CO_2/H_2 (1/1, 50 mL/min) and the DRIFTS spectra were continuously recorded. During the tests, the temperature was kept at 373 K for the whole measurement.

In situ DRIFTS of CO_2 and H_2 stepwise experiments, the catalyst (50 mg) was first activated in pure H_2 flow (25 mL/min) at 573 K (with linear heating to 573 K for 1 h and holding for 1 h). Following, the gas flow was switched to pure N_2 (40 mL/min) for 0.5 h until the system was cooled down to 373 K. After taking the background spectrum under N_2 atmosphere at 373 K, the CO_2 was admitted into the cell (25 mL/min) and the DRIFT spectra were continuously recorded for 1 h. Afterward, the reaction cell was purged by N_2 (30 mL/min) for 30 min to remove the CO_2 gas in the cell. Finally, H_2 (10 mL/min) was passed into the cell, while the DRIFTS spectra were recorded continuously. The system was maintained at 373 K for the whole measurement.

Thermal stability tests of catalysts. To investigate the stability of catalysts, the Pd/S-1-im and representative $PdMn_{0.6}$@S-1 catalysts were calcined under various atmospheres at high temperatures. (1) the Pd/S-1-im and $PdMn_{0.6}$@S-1 catalysts (0.1 g) were calcinated in flowing N_2 (40 mL/min) with linear heating to 700 °C for 2 h and holding for 2 h. (2) the $PdMn_{0.6}$@S-1 catalyst (0.1 g) was calcinated in flowing H_2 (40 mL/min) with linear heating to 700 °C for 2 h and holding for 2 h. (3) the $PdMn_{0.6}$@S-1 catalyst (0.1 g) was calcined in the O_2 and H_2 at 650 °C under the same treatment condition with N_2. Typically, the $PdMn_{0.6}$@S-1 catalyst was first calcinated in the

air at 650 °C (with linear heating to 650 °C for 2 h and holding for 2 h). following, the sample was then calcinated in H_2 at 650 °C under the same treatment condition with that in air. The above reduction and oxidation treatments were considered as once cycle. Totally, the $PdMn_{0.6}$@S-1 catalyst was calcinated up to 5 cycles.

CO_2 hydrogenation into formates. The CO_2 hydrogenation to formate reactions were performed in a batch reactor at 40 bar of gas pressure and 298 ~ 353 K. Typically, 2 mL of triethylamine/NaOH (1.5 M) solution was added into the reactor and then, 5 mg of catalyst was added into above solution and the solid catalyst was dispersed uniformly into the solution with the assistance of ultrasonic treatment for 1 min. Subsequently, the 40 bar of CO_2/H_2 (1/1) was pumped into the reactor (the air in the reactor should be aforehand removed by CO_2/H_2 forming gas). Finally, the reactor was placed into the oil-bath keeping at 298 ~ 353 K. After the completion of previous run, the catalyst was isolated from the reaction solution by centrifugation. The isolated catalyst was washed with water until the supernatant became neutral. The dried catalysts were reused in the catalytic CO_2 dehydrogenation. The spent catalysts were reused up to 5 consecutive catalytic cycles.

The hydrogenation of carbonates or bicarbonate reactions were also performed in a batch reactor at various H_2 pressures and concentrations of the carbonate or bicarbonate at 373 K. Typically, 2 mL of water was added into the reactor, and then 0.5 ~ 2.0 mmol of $NaHCO_3$ was added into the water and dissolved completely. Then, 5 mg of catalyst was added into above solution and the solid catalyst was dispersed uniformly into the solution with the assistance of ultrasonic treatment for 1 min. Subsequently, the H_2 gas with various pressures (10 ~ 40 bar) was injected into the reactor (the air in the reactor should be aforehand removed by H_2). Finally, the reactor was placed into the oil-bath keeping at 373 K.

The formate generation rate was calculated based on the total amount of Pd metal atoms in the catalysts. The calculation equation used was as below:

$$Rate = \frac{n_{formate}}{n_{Pd}t}$$

Where $n_{formate}$ and n_{Pd} are the molar ratios of generated formate and the total amount of Pd metal atoms (based on the ICP results) in the catalysts, and the t is the reaction time of the reaction in hours.

The TOF value was calculated based on based on the number of surface Pd atoms in catalysts. The calculation equation used was as below:

$$TOF = \frac{n_{formate}}{n_{surf\ Pd} t}$$

Where $n_{formate}$ and $n_{surf\ Pd}$ are the molar ratios of generated formate and the number of surface Pd atoms in the catalyst, and the t is the reaction time of the reaction in hours.

Dehydrogenation reaction of formic acid. The dehydrogenation reaction of formic acid was carried out using an apparatus containing a reaction unit and a gas collecting device. Typically, suitable amount of catalyst (molar ratios of n_{Pd}/n_{FA} were fixed at 0.012) and 1.0 mL of distilled water were first placed in a 25 mL two-necked round-bottomed flask, which was placed in a water bath with magnetic stirring (600 rpm) at a preset temperature (298 ~ 333 K) under ambient atmosphere. The volume of released gas was measured using a gas burette as well as an electronic balance recording the weight of excurrent water continuously. The reaction started when 0.5 mL of FA (6.0 M) aqueous solution was injected into the flask using a syringe. To evaluate the durability of catalysts, the representative $PdMn_{0.6}$@S-1 catalyst was isolated from the reaction solution by centrifugation and washed with water after the completion of a previous FA decomposition experiment and dried in the oven. The dried catalysts were then reused in the catalytic dehydrogenation of the FA solution at 333 K. After 5 consecutive catalytic cycles the spent catalyst was characterized using TEM.

The TOF is based on the number of surface Pd atoms in catalysts, which is calculated from the equation below:

$$TOF = \frac{P_{atm} V_{gas}/RT}{2\ n_{Pd} t}$$

Where P_{atm} is the atmospheric pressure (101.325 kPa), V_{gas} is the total final generated the volume of H_2 and CO_2, R is the universal gas constant (8.3145 m^3 Pa mol^{-1} K^{-1}), T is the room temperature (298 K), n_{Pd} is the mole number of surface Pd atoms in catalyst and t is the reaction time in hour.

Density Functional Theory Calculations. Periodic plane-wave density functional theory (DFT) calculations were carried out with the Vienna *ab initio* Simulation Package (VASP)[1, 2]. Core electronic states were represented by projector-augmented wave (PAW) pseudopotentials[3, 4], while valence electronic states were expanded with a plane-wave basis set with a cutoff energy of 520 eV. The Perdew-Burke-Ernzerhof (PBE) functional[5] was used to describe the effects of exchange and

correlation. Grimme's D3 correction[6] was applied to treat dispersion. All calculations were carried out with spin-polarization.

Pd and PdMn clusters were modeled in a cubic unit cell 20 Å on each side, ensuring at least 12 Å of vacuum to prevent spurious interactions between periodic images. The Brillouin zone was sampled at the gamma point only. Dipole corrections[7, 8] were applied in all directions to correct for electrostatic interactions between periodic images. Fermi surfaces were treated with Gaussian smearing with a smearing width of 0.01 eV to accelerate electronic convergence. Final energies were obtained by extrapolating the Fermi temperature to 0 K.

Transition state and geometry optimizations were considered converged when the maximum Hellmann–Feynman forces on all atoms were less than 0.02 eV/Å. Transition states were obtained using the climbing-image nudged elastic band (CI-NEB) method [9], with a minimum of 7 intermediate images excluding the initial and final state. All transition states were verified to have only one imaginary vibrational mode.

Harmonic vibrational frequencies were calculated by numerically differentiating the forces using a second-order finite differences approach with a step size of 0.007 Å. For these vibrational frequency calculations, all metal atoms and spectator species were fixed; only the adsorbate of interest was relaxed. The resulting Hessian matrix was then mass-weighted and diagonalized, yielding the normal mode frequencies.

First Principles Determination of Cluster Model for Pd-Mn Catalyst. We used *ab initio* molecular dynamics (AIMD) simulations to determine the most stable structures of 13-atom Pd-Mn clusters of various compositions near the experimentally optimal composition of $PdMn_{0.6}$. The AIMD simulations were performed in the *NVT* (canonical) ensemble using a Nosé–Hoover[10, 11] thermostat with a time step of 2 fs. In a simulated annealing procedure, the clusters were first heated up to 1500 K and then gradually cooled to 200 K over the span of ~5 ps. The lowest energy structures encountered in the AIMD simulations were then selected for geometry optimization. Using these structures, we constructed a convex hull from which we found Pd_8Mn_5 to be the ground state cluster (Figure S27).

XANES results for the Pd-Mn catalysts revealed that Mn had an oxidation state between +2 and +3, whereas Pd was slightly electron rich. To evaluate the oxidation states of Mn in our clusters, we first calculated the Mn Bader charges of bulk MnO (–1.40 e^-) and Mn_2O_3 (–1.78 e^-) using the

algorithm developed by Henkelman and coworkers[12-14]. Their Bader charges were then used to calibrate a mapping between the formal oxidation states of Mn and their computed Bader charges. For these bulk calculations, the Brillouin zone was sampled with Monkhorst Pack[15] k-point mesh with a reciprocal k-points density of 192 k-points / Å^3. Hubbard U corrections[16] for Mn with a value of 3.90 eV were applied[17]. D3 corrections were not applied, since the U corrections were specifically parameterized from pure PBE calculations[18]. Note that Hubbard U corrections were not applied for clusters since previous studies found that DFT+U was not needed for small Mn oxide clusters[19]. This also ensures a fair comparison between the Pd and PdMn clusters.

From the Mn Bader charges of Pd_8Mn_5, the oxidation state of Mn in the clean Pd_8Mn_5 cluster was significantly less than +2. A more realistic model for the Pd-Mn catalyst is likely an oxidized Pd_8Mn_5 cluster covered by a number of O* and OH* species (* denotes binding to the cluster). We thus sought to determine the most experimentally realistic coverage of O* and OH* by screening clusters with different coverages of O* and OH* (Figure S28). For each of these coverages, we again performed AIMD simulations to find the most stable structure. All atoms, including Pd and Mn, were unfixed to account for possible cluster reconstructions. Due to the high computational cost of this approach, we only studied coverages of nO* + mOH*, where the maximum n+m is 15 (Figure S28a).

After determining the most stable structures for each coverage, we then constructed phase diagrams for the O* and OH* decorated Pd-Mn clusters with respect to the chemical potentials of H_2 and H_2O, as expressed in terms of their gas phase partial pressures (Figure S28c). For the phase diagram, the free energies of the most stable clusters at each coverage were used. Components of the free energies, including the zero-point energy, finite-temperature corrections to the enthalpy, and entropies, were calculated from statistical thermodynamics using the vibrational frequencies of the O* and OH* species on the clusters[20]. The frequencies were calculated with all Pd and Mn atoms fixed and all O and H atoms relaxed.

Under experimental conditions (333 K, 0.1 M FA), the reaction solution has a pH of approximately 2.4 (note that the K_a of formic acid changes minimally between room temperature and 333 K)[21]. By the Nernst equation, the H chemical potential at this pH is equal to that of H_2(g) at a partial pressure of 2×10^{-5} bar. Additionally, the saturation vapor pressure of water at 333 K is

2×10^{-1} bar. At these conditions, we determined from our phase diagram that the thermodynamically most favorable coverage is 1O* +13OH*. The same coverage is also found under conditions of the XAS measurements (Figure S28c)

The $Pd_8Mn_5O(OH)_{13}$ cluster has a Mn oxidation state of between +2 and +3, in line with our XANES results. The Pd atoms of $Pd_8Mn_5O(OH)_{13}$ are, however, slightly electron deficient (by 0.04 e^-). This discrepancy with the XANES results showing slight electron enrichment of Pd is likely within the error bars of our calculations and may also be caused by factors such as the lack of modelling of the support. Out of all the oxidized clusters we studied, $Pd_8Mn_5O(OH)_{13}$ is one of the clusters that most closely meet both the criteria of Mn having an oxidation state between +2 and +3, and Pd being electron rich (Figure 28b), thus providing further support for our choice of model.

Calculation of Generalized Coordination Number. The Generalized Coordination Number[75] for atom *i* in a cluster (GCN_i) with *n* neighbors was calculated as:

$$GCN_i = \sum_{j=1}^{n} \frac{CN_j}{CN_{max}},$$

where *j* is the index of a neighboring atom, CN_j is the coordination number of the neighbor, and CN_{max} is a constant representing the coordination number of an atom in the bulk. We used a value of CN_{max} = 12 (fcc crystal). Neighbors were defined as any atoms within 3.3 Å of the considered atom. Only metal atoms (Pd and Mn) were considered in the calculation of the GCN.

Supplementary Figures and Tables

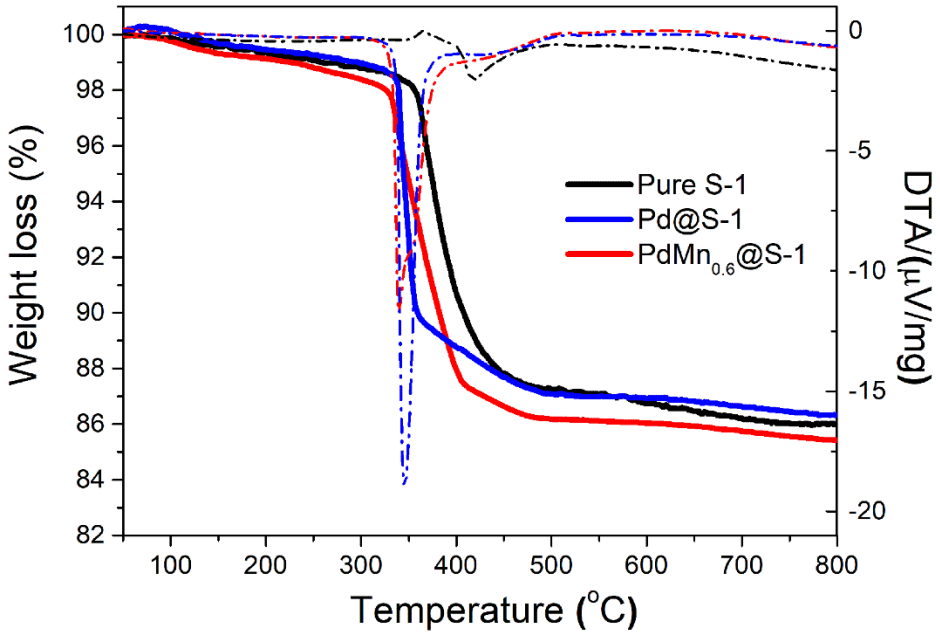

Figure S1. TG/DTA curves of pure S-1, Pd@S-1, and $PdMn_{0.6}$@S-1 catalysts without calcination.

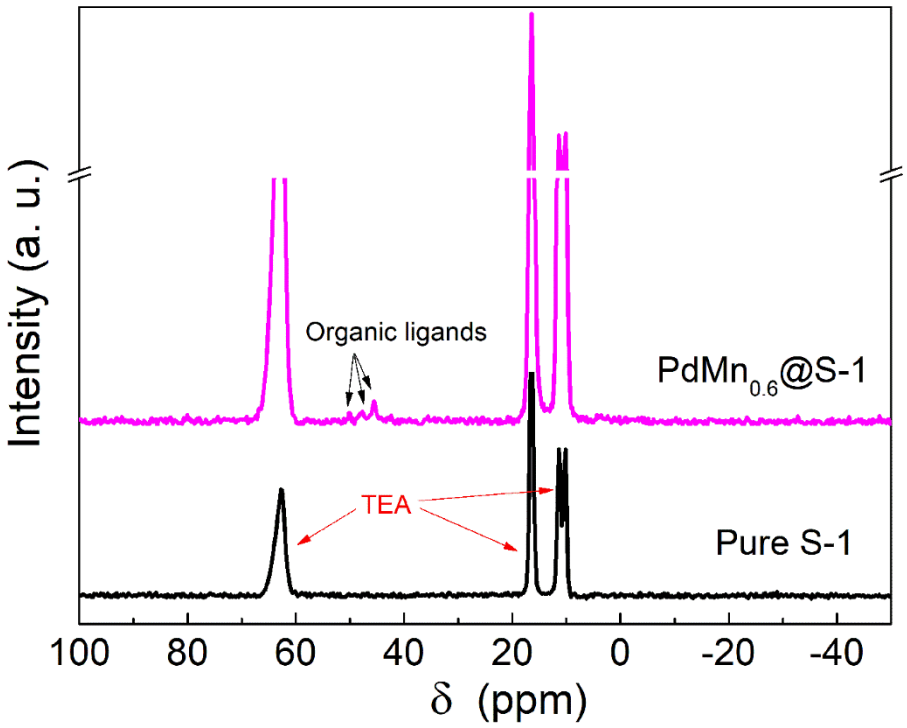

Figure S2. ^{13}C MAS NMR spectra of $PdMn_{0.6}$@S-1 and pure S-1 catalysts without calcination.

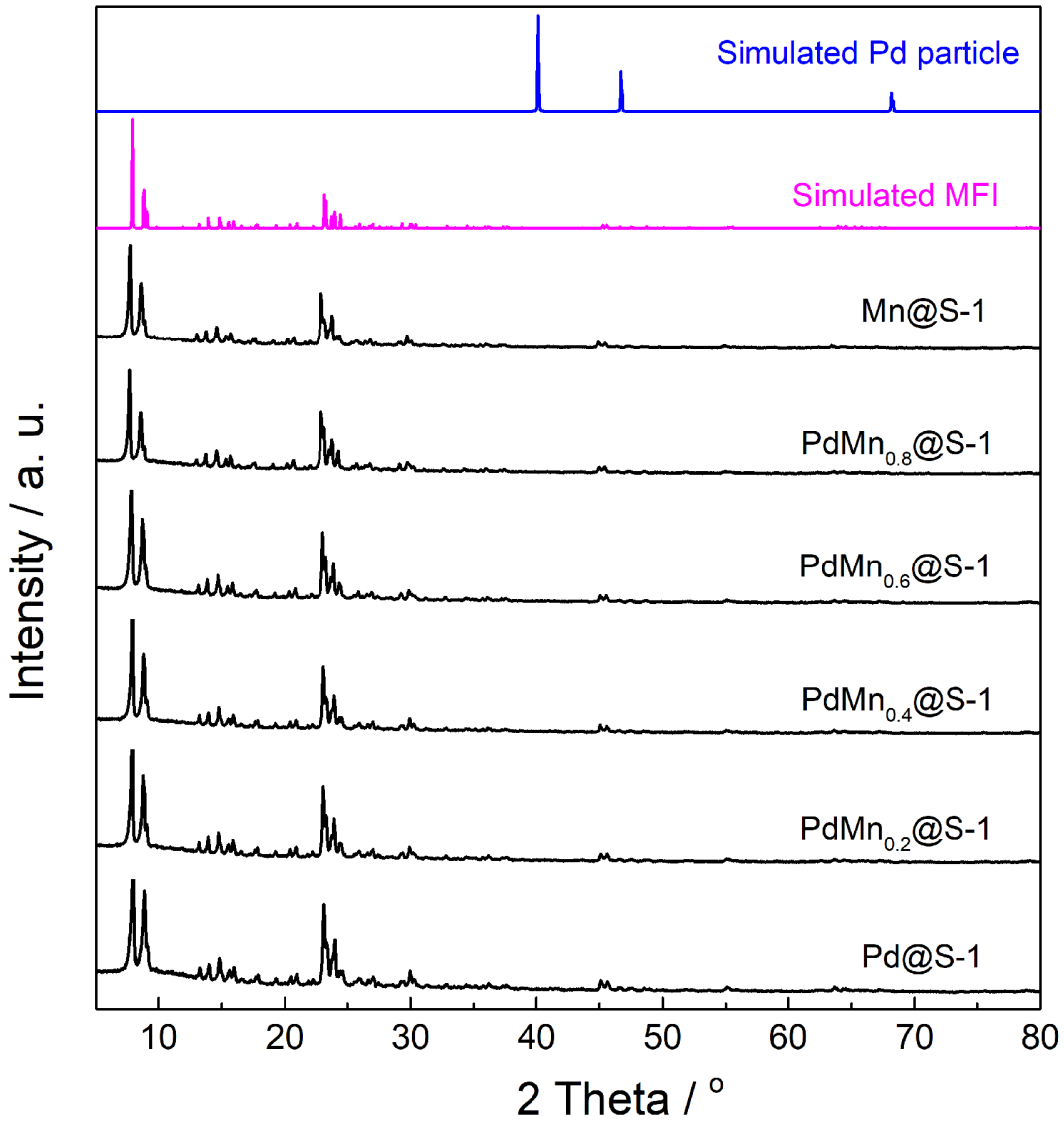

Figure S3. XRD patterns of the Pd@S-1, Mn@S-1 and $PdMn_x$@S-1 catalysts with various Pd/Mn ratios as well as simulated **MFI** zeolite and Pd particle.

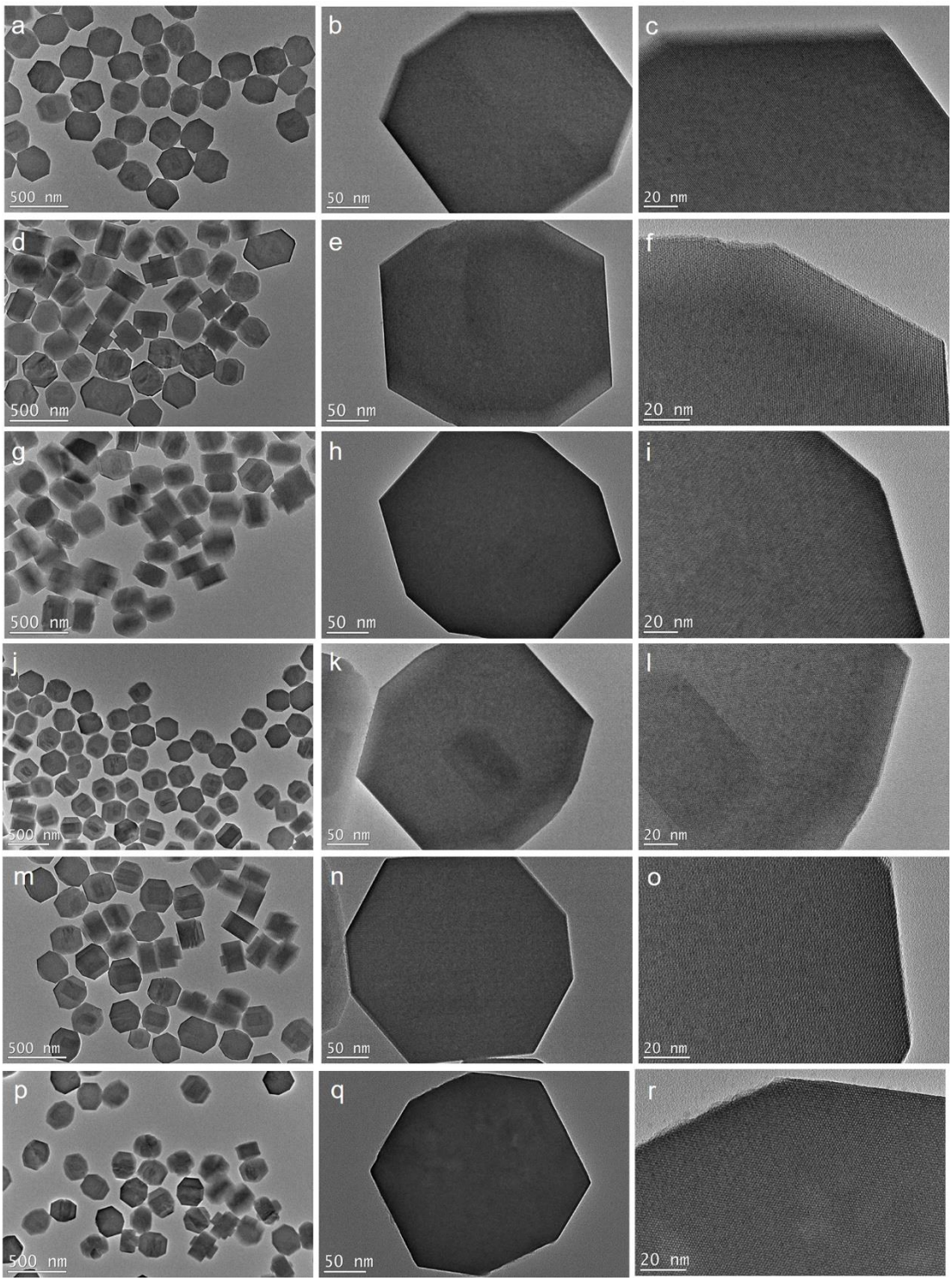

Figure S4. TEM images of (a-c) Pd@S-1, (d-f) $PdMn_{0.2}$@S-1, (g-i) $PdMn_{0.4}$@S-1, (j-l) $PdMn_{0.6}$@S-1, (m-o) $PdMn_{0.8}$@S-1 and (p-r) Mn@S-1 catalysts.

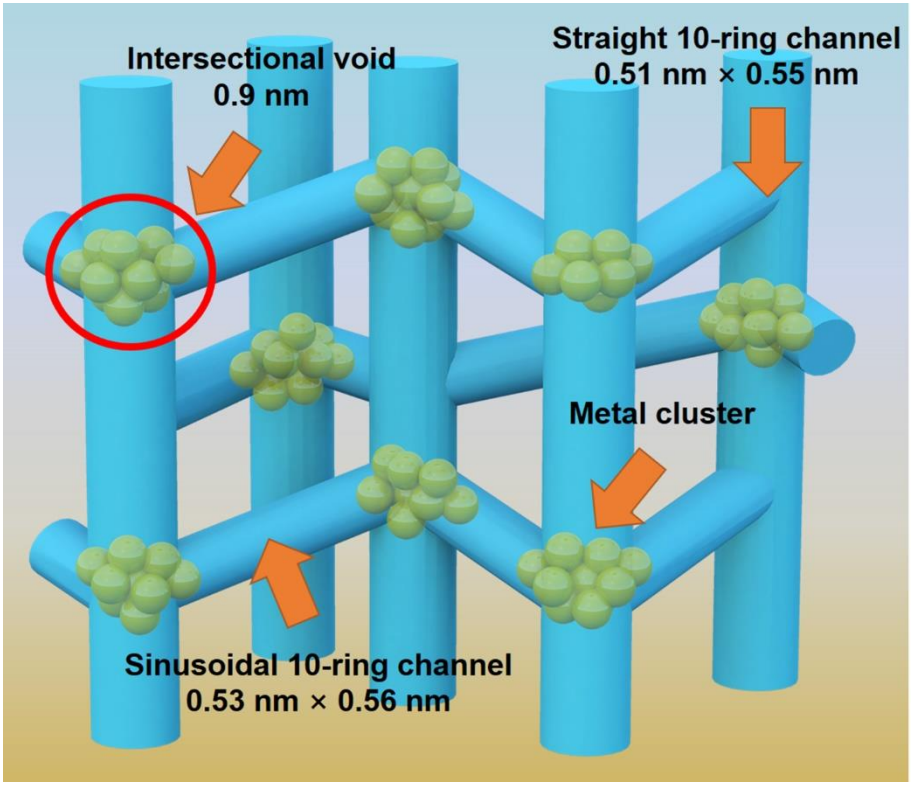

Figure S5. Schematic illustration of the location of sub-nanometer metal clusters confined within MFI zeolite channels.

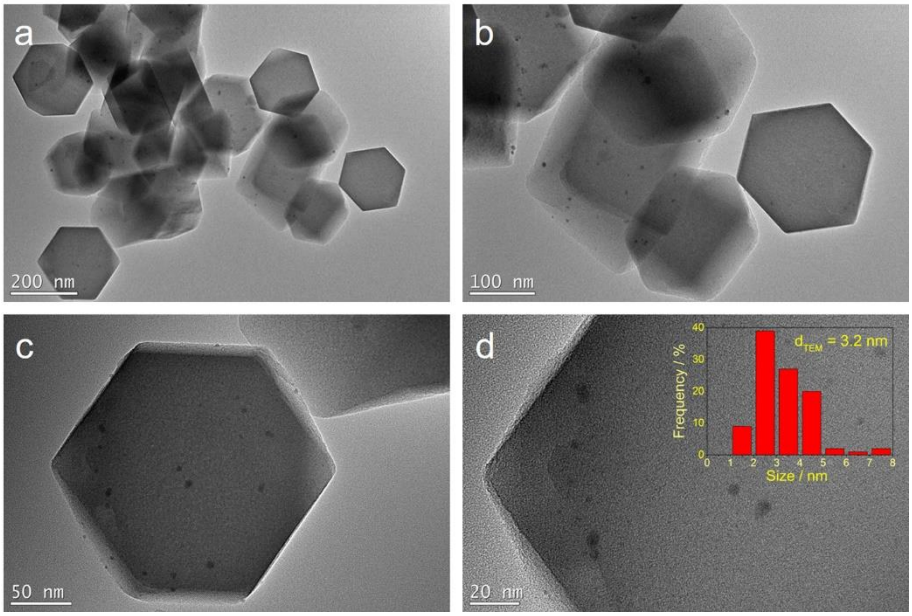

Figure S6. TEM images of the Pd/S-1-im sample.

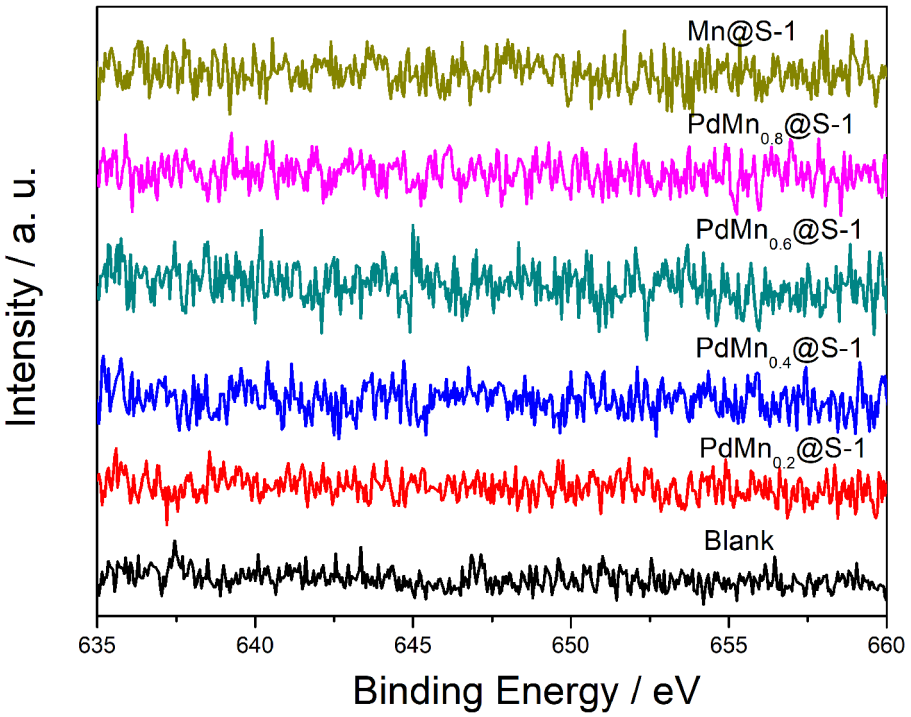

Figure S7. Mn 2p XPS spectra of Mn@S-1, $PdMn_{0.2}$@S-1, $PdMn_{0.4}$@S-1, $PdMn_{0.6}$@S-1, and $PdMn_{0.8}$@S-1 catalysts.

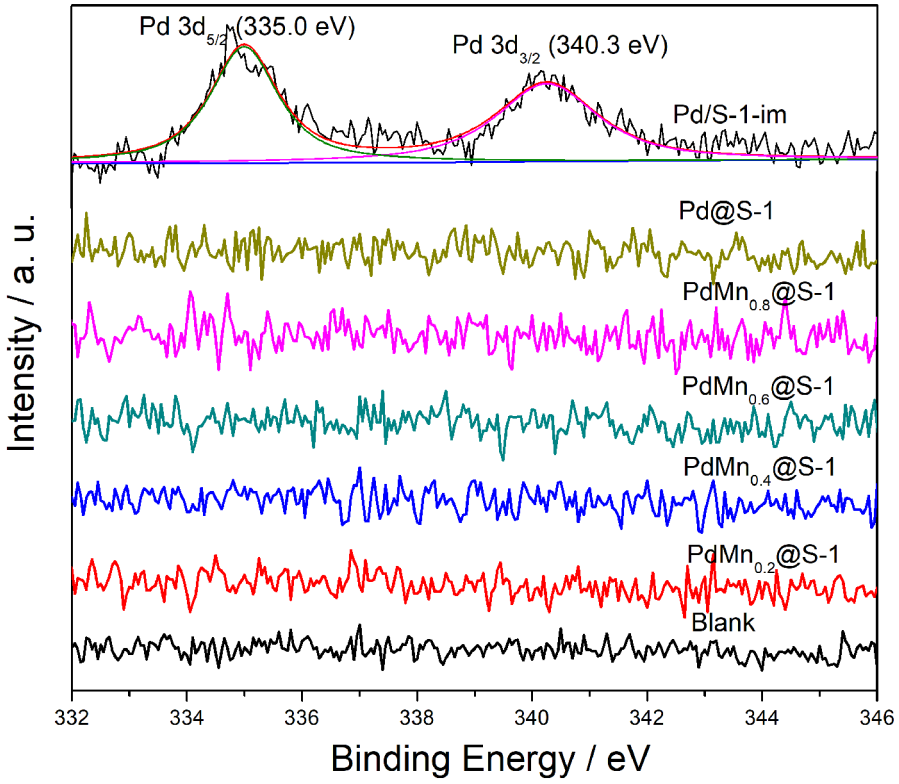

Figure S8. Pd 3d XPS spectra of Pd@S-1, $PdMn_{0.2}$@S-1, $PdMn_{0.4}$@S-1, $PdMn_{0.6}$@S-1, $PdMn_{0.8}$@S-1, and Pd/S-1-im catalysts.

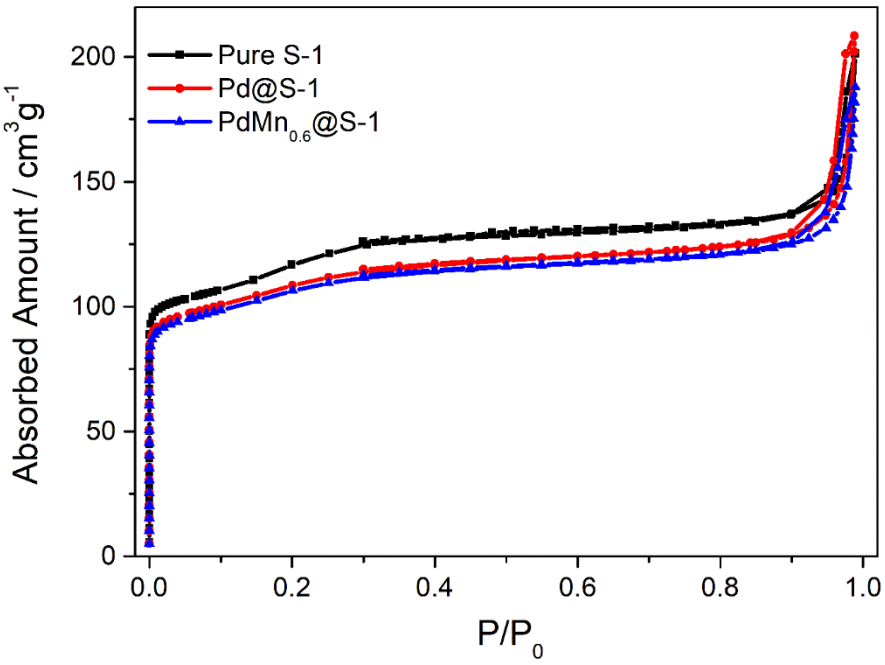

Figure S9. N_2 adsorption/desorption isotherms of pure S-1, Pd/S-1, and $PdMn_{0.6}$@S-1 catalysts.

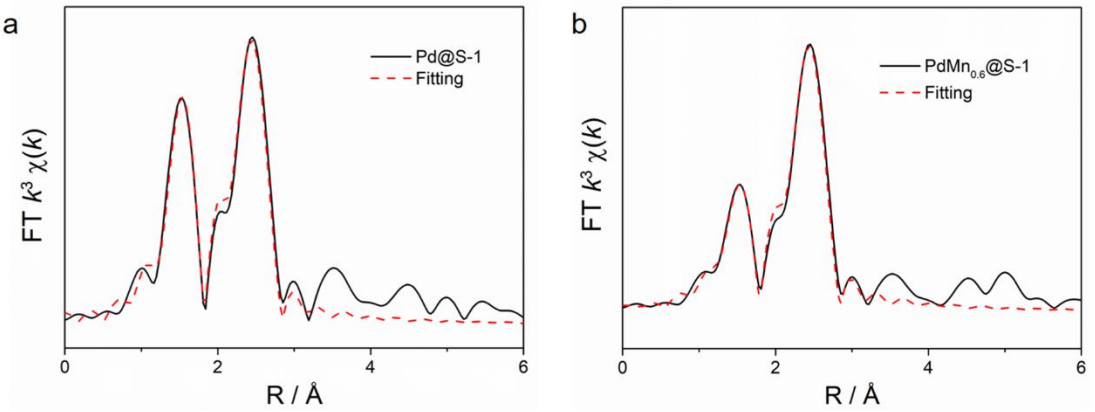

Figure S10. Fourier transform of k^3-weighted EXAFS spectra of (a) Pd@S-1 and (b) $PdMn_{0.6}$@S-1.

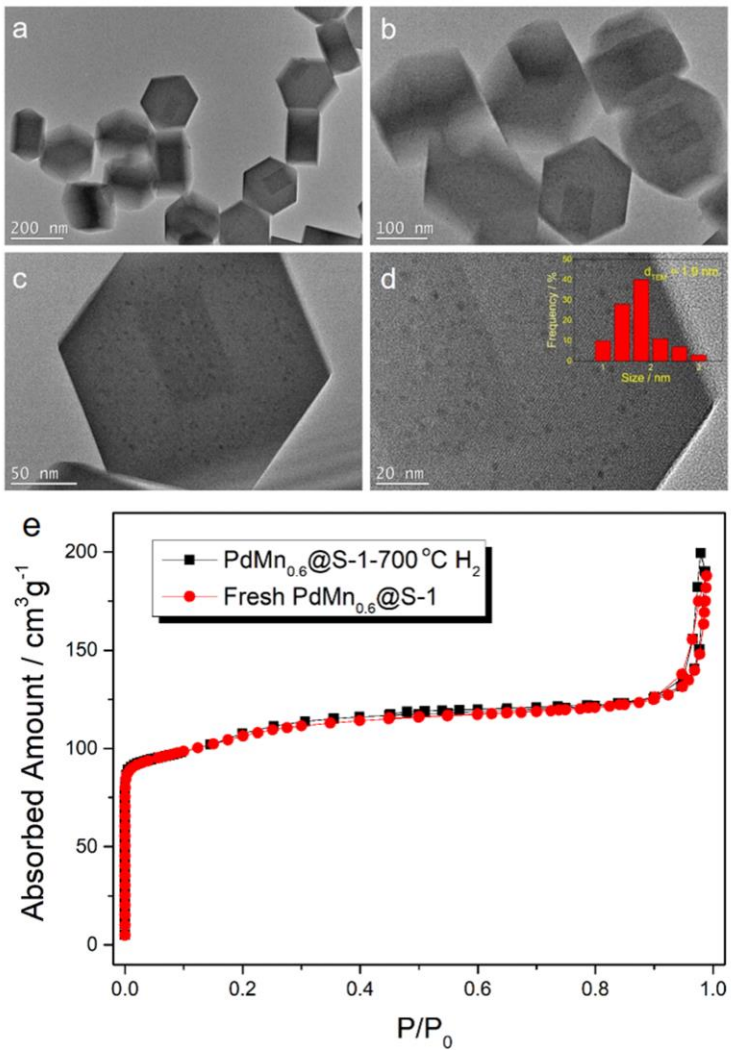

Figure S11. (a-d) TEM images of $PdMn_{0.6}$@S-1 after calcination at 700 °C for 2 h under H_2 atmosphere. (e) N_2 adsorption/desorption isotherms of $PdMn_{0.6}$@S-1 and $PdMn_{0.6}$@S-1 after calcination at 700 °C for 2 h under H_2 atmosphere. The microporous area and volume of PdMn0.6@S-1-700 °C H_2 catalyst are 146 m^2/g and 0.101 cm^3/g, respectively, which are much the same as those of fresh $PdMn_{0.6}$@S-1 catalysts. The above results indicate that the zeolite micropores are not destroyed and the aggregated metal species are located within the adjacent channels/micropores.

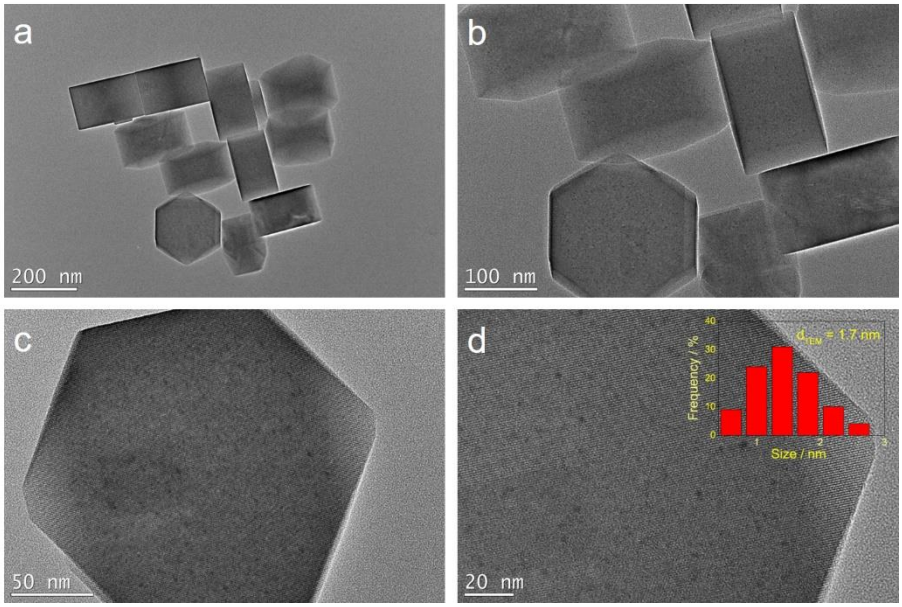

Figure S12. TEM images of $PdMn_{0.6}$@S-1 after calcination at 700 °C for 2 h under N_2 atmosphere.

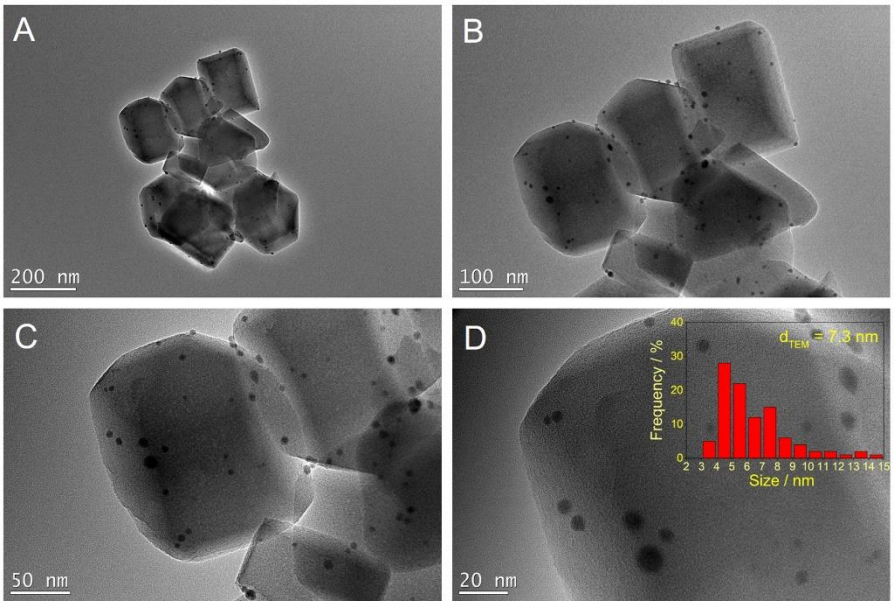

Figure S13. TEM images of Pd/S-1-im after calcination at 700 °C for 2 h under N_2 atmosphere.

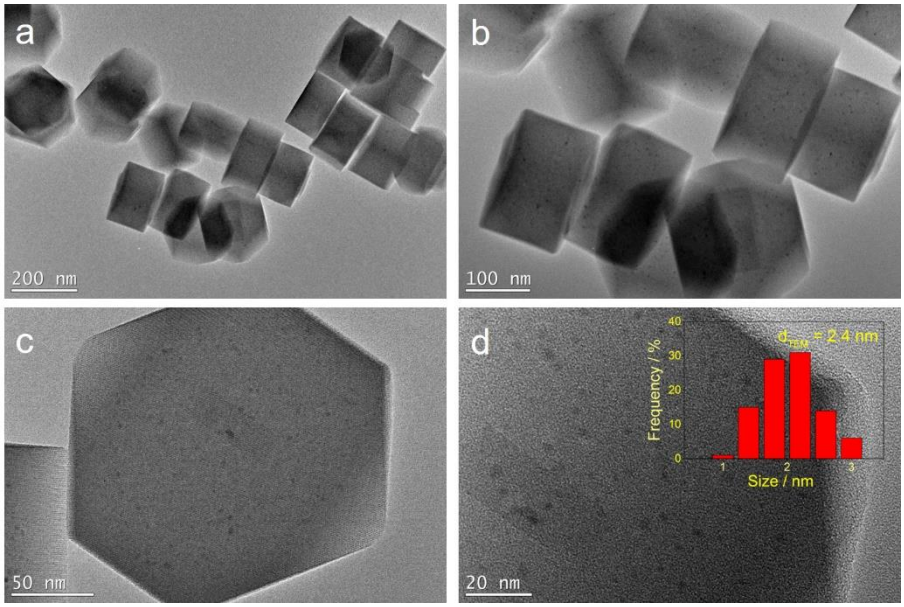

Figure S14. TEM images of $PdMn_{0.6}$@S-1 after one cycle of oxidation-reduction treatment at 650 °C for 2 h.

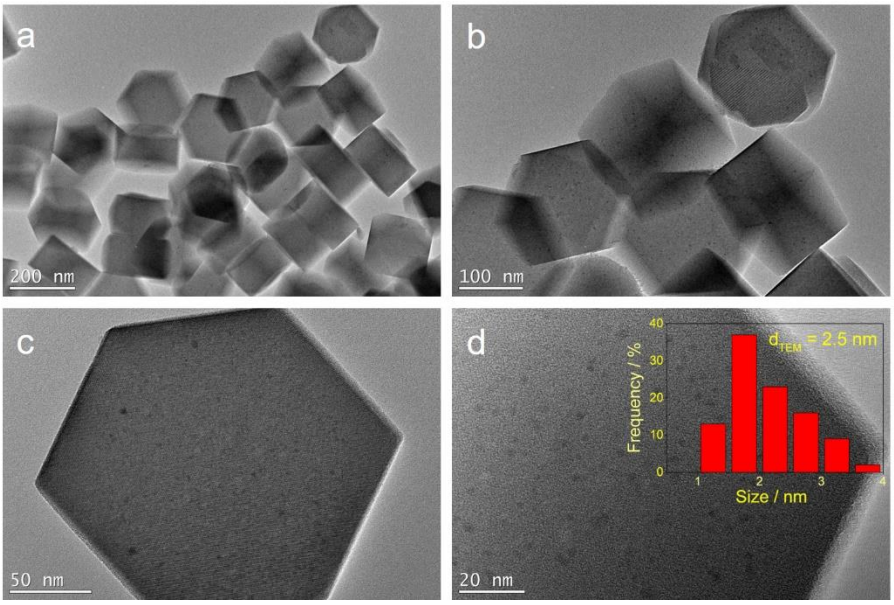

Figure S15. TEM images of $PdMn_{0.6}$@S-1 after five cycles of oxidation-reduction treatment at 650 °C for 2 h.

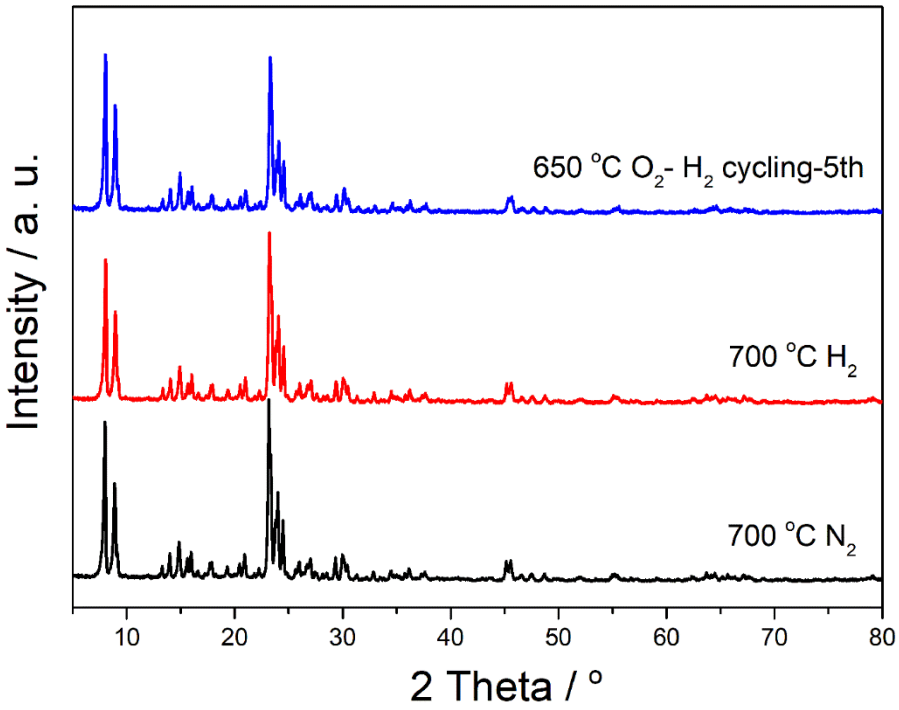

Figure S16. XRD patterns of $PdMn_{0.6}$@S-1 after calcination under various atmospheres.

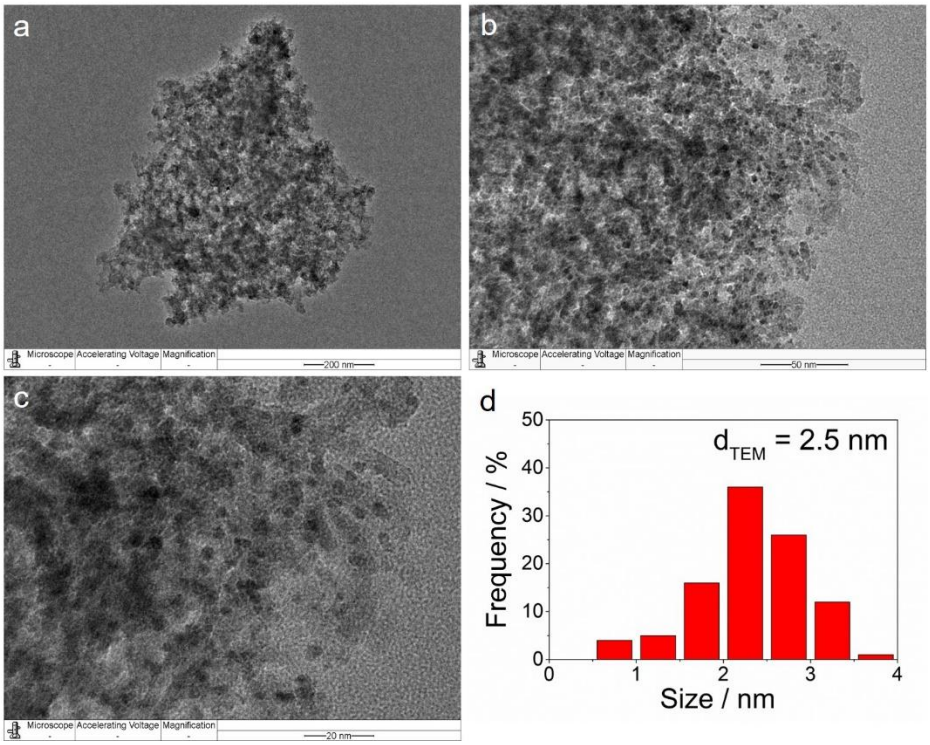

Figure S17. TEM images and corresponding size distribution of commercial Pd/Al_2O_3 catalysts.

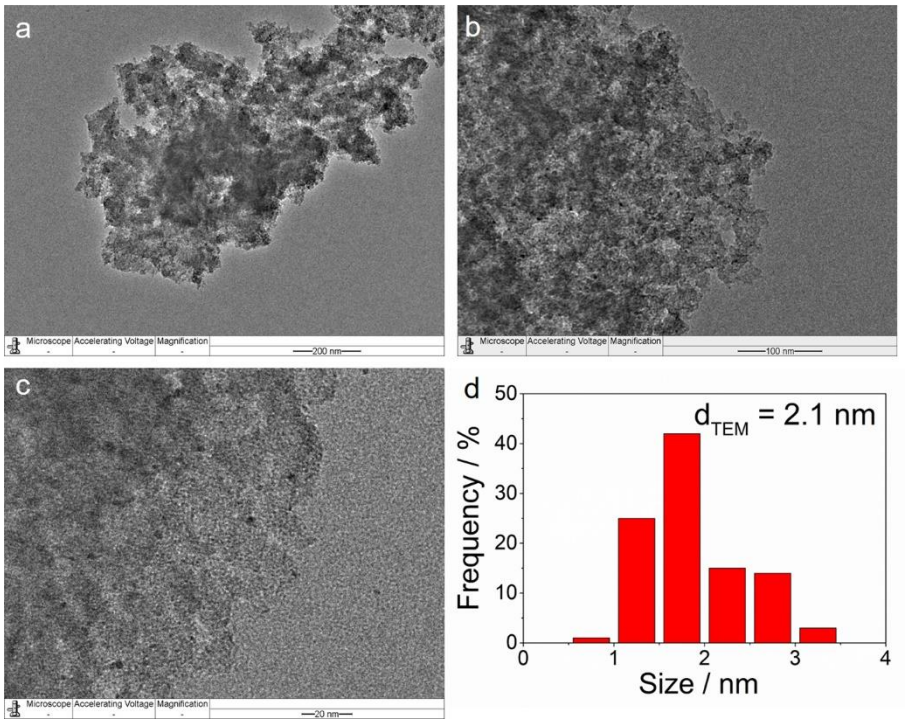

Figure S18. TEM images and corresponding size distribution of commercial Pd/C catalysts.

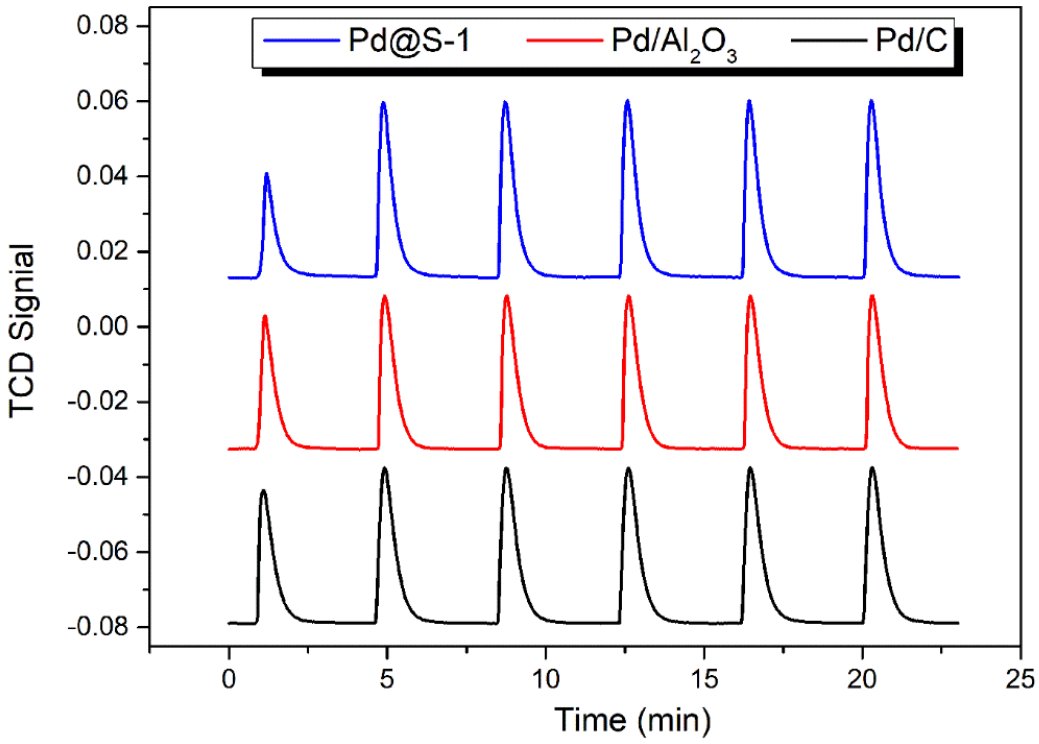

Figure S19. H_2 pulse chemisorption profiles of Pd@S-1, Pd/C, and Pd/Al_2O_3 samples.

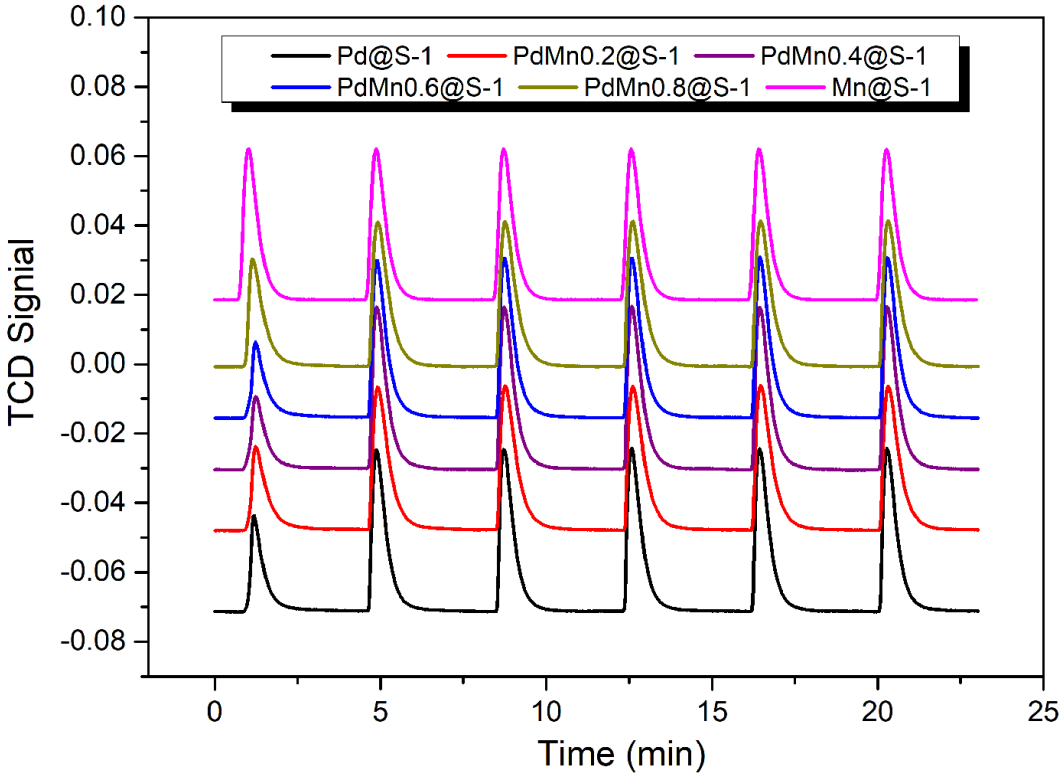

Figure S20. H_2 pulse chemisorption profiles of Pd@S-1 and $PdMn_x$@S-1 samples.

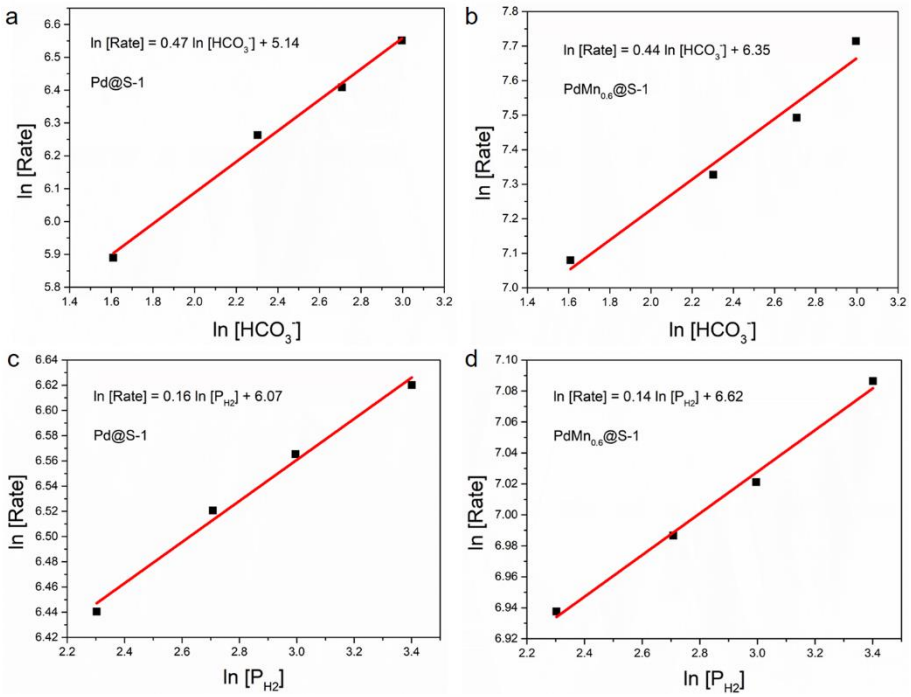

Figure S21. Effect of $NaHCO_3$ concentrations (1 ~ 2.5 mmol of $NaHCO_3$, 2.0 MPa initial H_2 pressure at 373 K) on the $NaHCO_3$ hydrogenation into formate catalyzed by (a) Pd@S-1 and (b) $PdMn_{0.6}$@S-1 catalyst. Effect of initial H_2 pressure (2 mmol of $NaHCO_3$, 10 mg catalyst, 10 ~ 30 bar initial H_2 pressure at 373 K) on the $NaHCO_3$ hydrogenation catalyzed by (c) Pd@S-1 and (d) $PdMn_{0.6}$@S-1 catalyst.

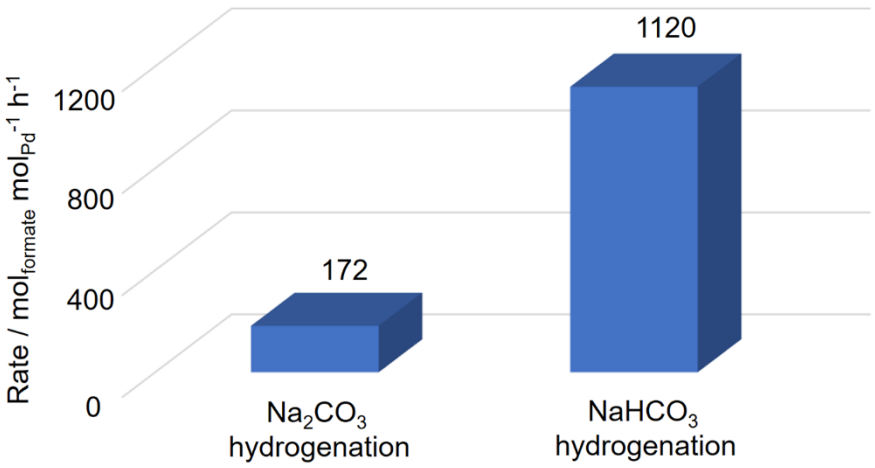

Figure S22. Formate generation rates from the hydrogenation of Na_2CO_3 and $NaHCO_3$ over the $PdMn_{0.6}$@S-1 catalyst. Conditions: catalyst (5 mg), 1 M aqueous solution of Na_2CO_3 and $NaHCO_3$ (2 mL), 20 bar of H_2, 373 K.

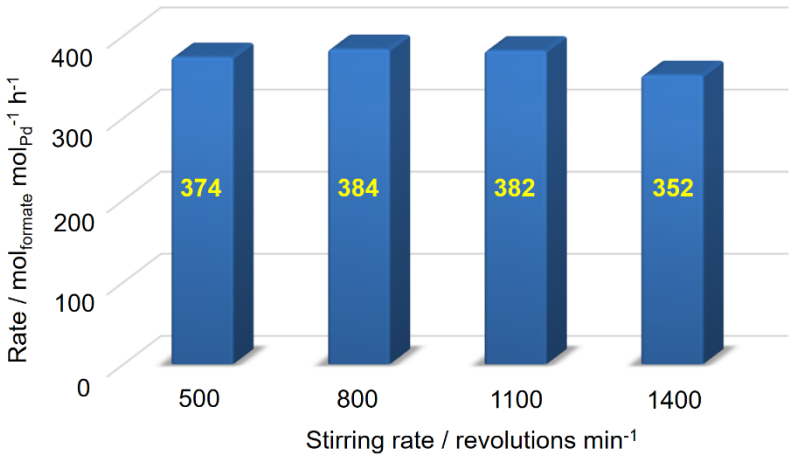

Figure S23. Comparison of the formate generation rates from the CO_2 hydrogenation over the $PdMn_{0.6}$@S-1 catalyst with different stirring rates. Conditions: catalyst (5 mg), 1.5 M aqueous NEt_3 solution (2 mL), H_2/CO_2 (1:1, 40 bar), 298 K, stirring rate: 500 ~ 1400 revolutions min^{-1}.

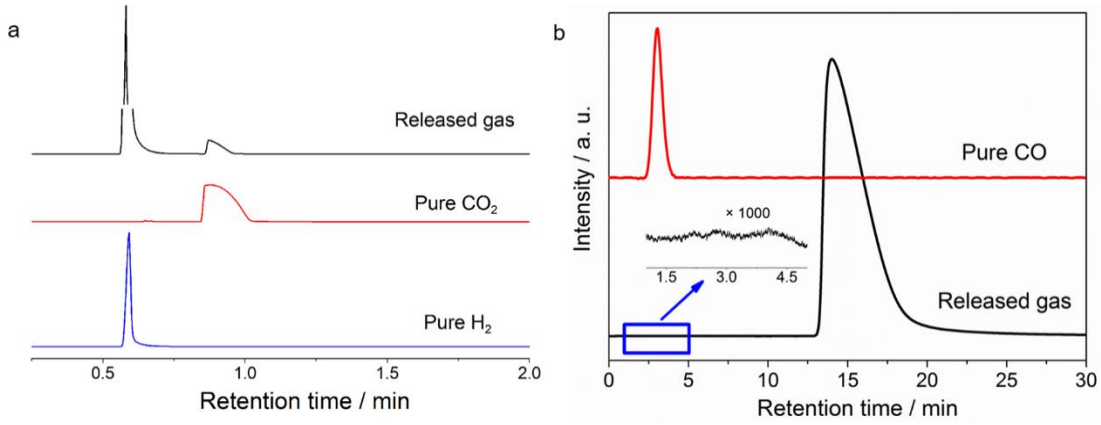

Figure S24. GC spectra (a) TCD detector and (b) FID detector of the released gas from the decomposition of FA solution over the $PdMn_{0.6}$@S-1 catalyst at 333 K.

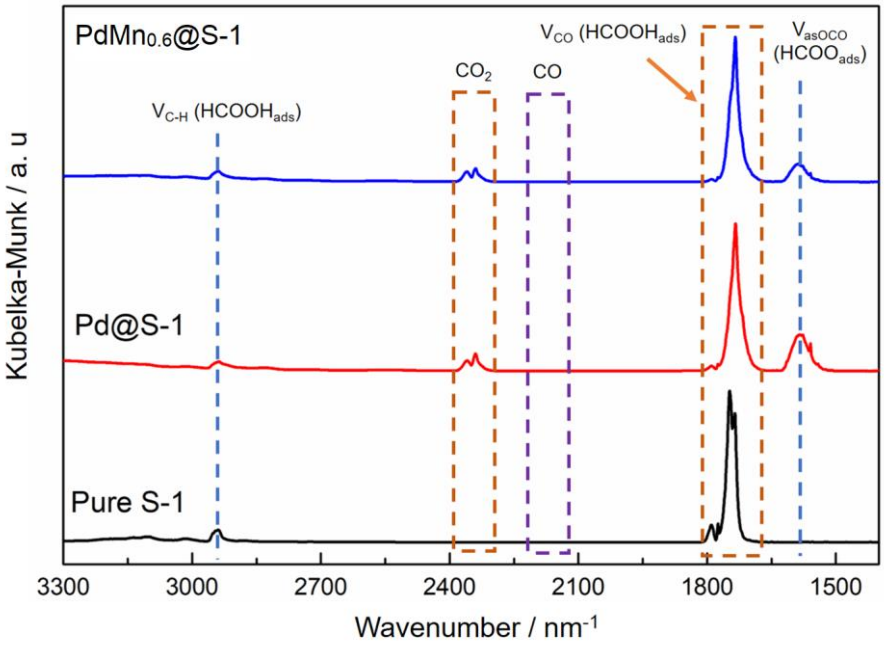

Figure S25. In situ DRIFTS spectra of FA dehydrogenation reactions were performed over Pd@S-1, $PdMn_{0.6}$@S-1 and Pure S-1 catalysts at 333 K. All catalysts were first activated by pure H_2 at 573 K for 1 h and then the temperature decreased to 333 K and the reaction cell was purged with pure N_2 for 0.5 h. Following, the FA were introduced into the reaction cell. The DRIFTS spectra of all catalysts were taken after introducing FA for 5 min.

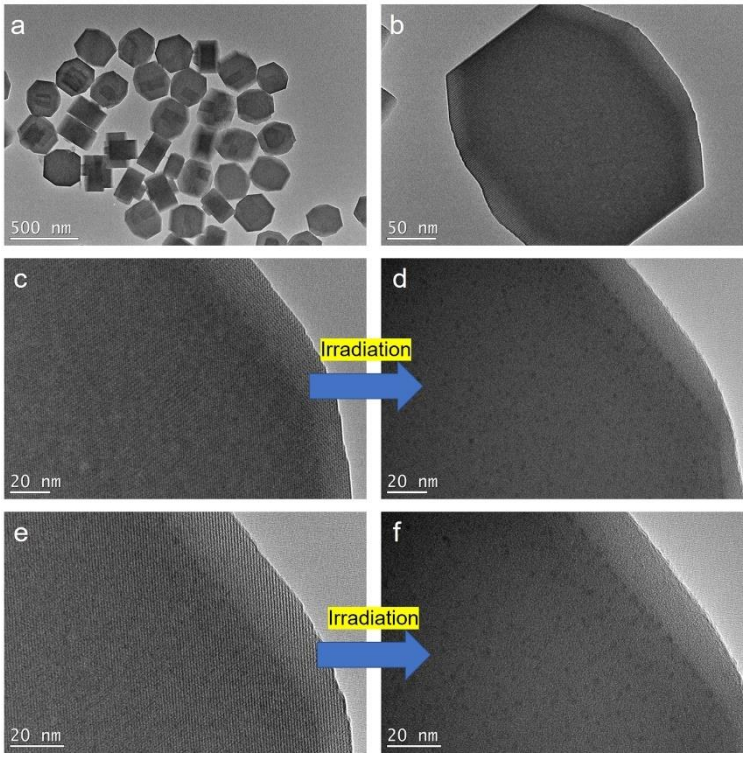

Figure S26. TEM images of $PdMn_{0.6}$@S-1 catalyst after 5th durability tests at 333 K.

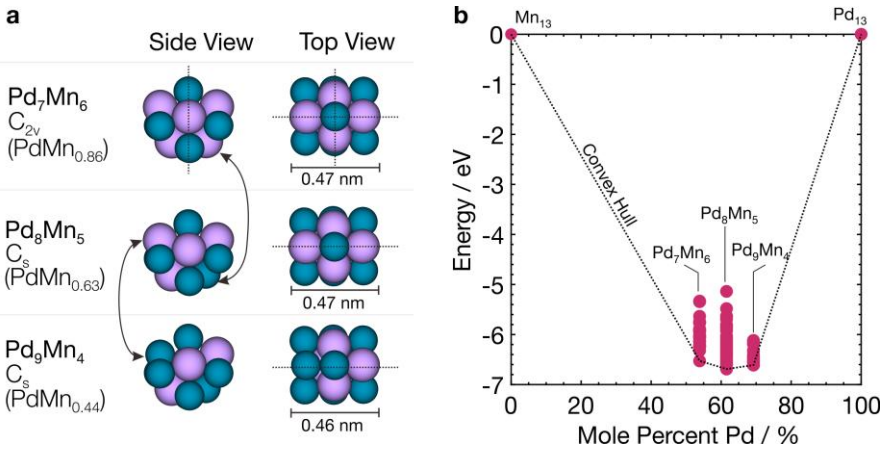

Figure S27. Determining the ground state composition of 13-atom Pd-Mn clusters. Three compositions near the experimental composition of $PdMn_{0.6}$ were probed—Pd_7Mn_6, Pd_8Mn_5, and Pd_9Mn_4. (a) The most stable structures of Pd-Mn clusters found via *ab initio* molecular dynamics (AIMD) simulations. The point group of each cluster is given in Schoenflies notation. Dashed lines mark symmetry planes. Notice that very similar structures were obtained for all three compositions. Arrows mark where swapping a Pd for a Mn atom interconverts a pair of structures. Color code: blue – Pd, purple – Mn. (b) Convex hull (dotted line) of Pd-Mn clusters. Each red dot represents a different cluster structure obtained from AIMD simulations. Energies are calculated with respect to the most stable structures of Mn_{13} (an icosahedron; see *Phys. Rev. B* **83**, 075425 (2011)) and Pd_{13} (bilayer structure; see Figure 7 in main text). More negative energies indicate higher stability.

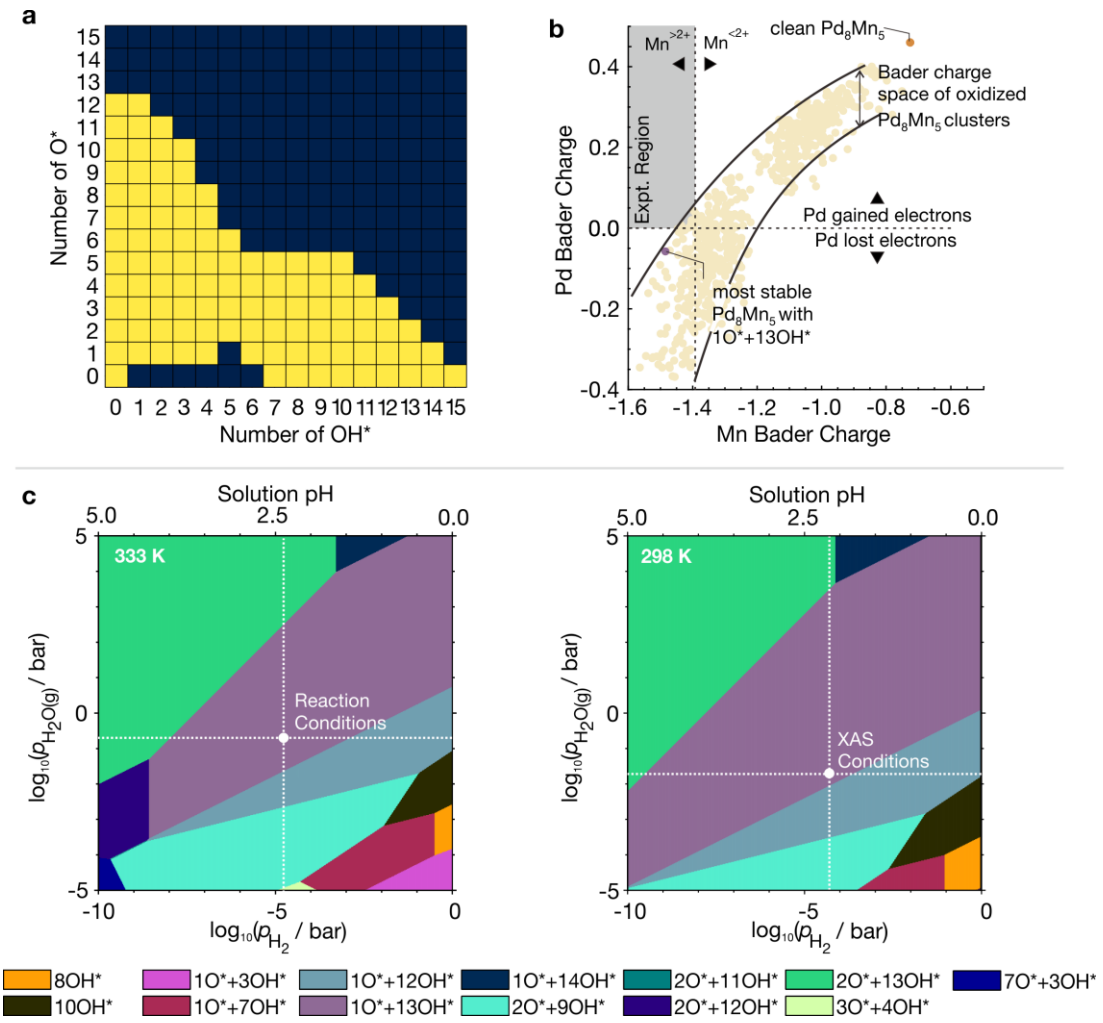

Figure S28. Determining the ground state coverage of O* and OH* on Pd_8Mn_5. (a) Illustration of the probed (yellow) and unprobed (dark blue) coverages. (b) Mn and Pd Bader charges, averaged over all Mn and Pd atoms, for Pd_8Mn_5 clusters with various coverages of O* and OH*. Each point represents a different cluster obtained from *ab initio* molecular dynamics simulations. Positive (negative) Bader charge indicates gain (loss) of electrons. Points in the grey shaded region are consistent with the experimental observations of Mn having a valence between +2 and +3 and Pd gaining electrons. Black lines are a guide for the eye marking out the space of possible Bader charges. Note that the correlation between Pd and Mn Bader charges make it difficult to fulfil both experimental criteria. Clean Pd_8Mn_5 and the most stable cluster under experimental and XAS conditions (see part (c)) are marked out. (c) Phase diagram of O* and OH* coverages on Pd_8Mn_5 computed at 333 K (left) and 298 K (right). Only the most stable structure for each coverage was considered. Reaction conditions (333 K, 0.1 M FA solution) and EXAFS conditions (298 K, atmospheric conditions) are marked out on the respective plots. Reaction conditions correspond to $p(H_2O) = 2\times10^{-1}$ bar (based on the saturation H_2O vapor pressure at 333 K) and $p(H_2) = 2\times10^{-5}$ bar (based on the solution pH of 2.4). XAS conditions correspond to $p(H_2O) = 3\times10^{-2}$ bar (based on the saturation H_2O vapor pressure at 298 K) and $p(H_2) = 5\times10^{-5}$ bar (based on abundance of H_2 in air).

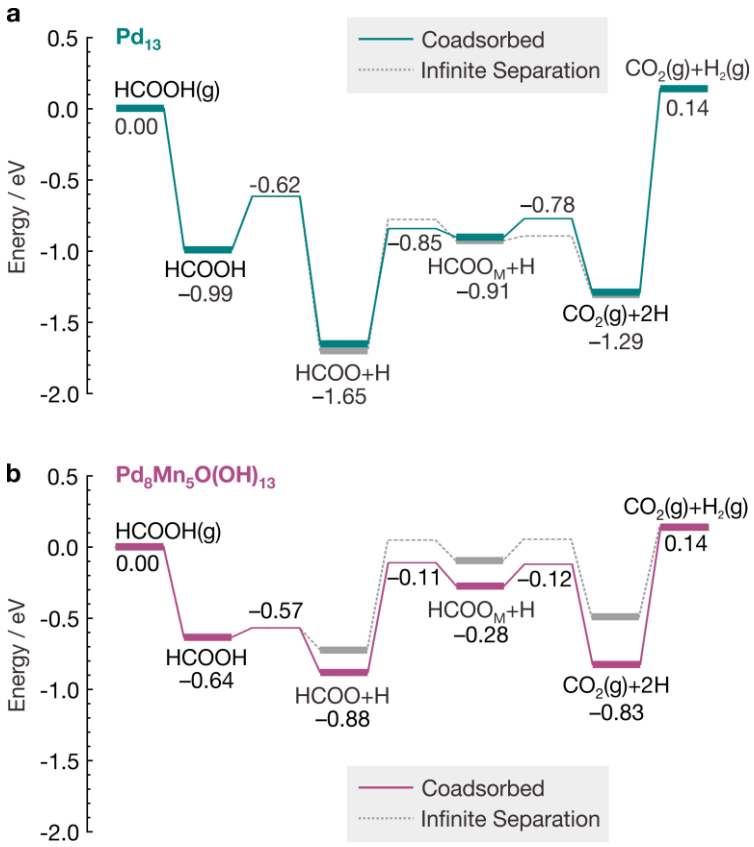

Figure S29. Potential energy diagrams (PEDs) for FA decomposition, where energetics were calculated with the coadsorption of adsorbates. (a) PED for Pd_{13} (b) PED for $Pd_8Mn_5O(OH)_{13}$. Each state is labelled by its energy, which is referenced to the initial state of the clean cluster and HCOOH(g). Bold lines indicate minima, whereas thin lines indicate transition states. Energetics calculated at infinite separation are shown in dotted grey lines for reference; the energies of these infinitely separated states are not labelled. $HCOO_M$ refers to a monodentate HCOO intermediate (as opposed to the more stable bidentate HCOO intermediate).

Table S1. Metal loadings and porosity of the catalysts.

Sample	Pd loading [a] (wt %)	Mn loading [a] (wt %)	Molar ratio of Pd/Mn [a]	S_{BET} [b] (m^2/g)	S_{micro} [c] (m^2/g)	S_{ext} [c] (m^2/g)	V_{micro} [c] (cm^3/g)	Metal dispersion [d]
Pure S-1	0	0	—	418	268	150	0.111	-
Pd@S-1	0.63	0	—	398	251	147	0.102	94.2%
$PdMn_{0.2}$@S-1	0.61	0.07	0.22	—	—	—	—	84.7%
$PdMn_{0.4}$@S-1	0.60	0.13	0.42	—	—	—	—	84.6%
$PdMn_{0.6}$@S-1	0.59	0.16	0.53	389	247	142	0.101	81.9%
$PdMn_{0.8}$@S-1	0.59	0.21	0.69	—	—	—	—	53.8%
Mn@S-1	0	0.25	—	—	—	—	—	0%

[a] Analyzed by inductively coupled plasma atomic emission spectroscopy (ICP-AES). [b] S_{BET} (total surface area) calculated by applying the BET equation using the linear part ($0.05<P/P_0<0.30$) of the adsorption isotherm. [c] S_{micro} (micropore area) and S_{ext} (external surface area) calculated using the *t*-plot method. [d] Metal dispersions obtained from H_2 chemisorption measurements.

Table S2. EXAFS parameters of Pd@S-1 and $PdMn_{0.6}$@S-1 catalysts as well as Pd foil and PdO standards.

Sample	Shell	CN	R	△E
PdO	Pd-O	4	2.018±0.010	-0.4±1.6
Pd foil	Pd-Pd	12	2.744±0.001	-5.4±0.2
Pd@S-1	Pd-O	2.0±0.2	2.001±0.007	-2.7±1.26
	Pd-Pd	3.8±0.3	2.731±0.004	-7.3±0.6
$PdMn_{0.6}$@S-1	Pd-O	1.7±0.2	1.998±0.013	-4.3±2.0
	Pd-Pd (Mn)	4.7±0.3	2.725±0.004	-7.7±0.5

CN, coordination number; R, the distance between absorber and backscatter atoms.

Table S3. Comparisons of catalytic activities for the formate generation from CO_2 hydrogenation catalyzed by previously reported heterogeneous catalysts with that synthesized in this work.

Catalysts	T/K	P_{CO2}/P_{H2} (bar)	Solution	Rate[a] $mol_{formate}$ $mol_{metal}^{-1}h^{-1}$	Reference
$PdMn_{0.6}$@S-1	**298**	**20/20**	**NEt_3**	**382**	**This Work**
	298	**20/20**	**NaOH**	**526**	
	353	**20/20**	**NEt_3**	**1265**	
	353	**20/20**	**NaOH**	**2151**	
2%Pd/ZrO_2-T	373	20/20	$NaHCO_3$	671	22
Au/SiO_2-Schiff	353	50/30	NEt_3/mathanol	938	23
	333	50/30	NEt_3/mathanol	195	
Pd/mpg-C_3N_4	423	27/13	NEt_3	3.6	24
IrPN/SBA-15	333	20/20	NEt_3	175	25
Ru/LDH (Mg^{2+}/Al^{3+}=5)	373	10/10	NaOH	29	26
Pd@Ag/TiO_2	373	10/10	$NaHCO_3$	104	27
0.66%Ir/AP-POP	383	40/40	NEt_3	1047	28
PdAg/SBA-15	373	10/10	$NaHCO_3$	36	29
Au NP/Al_2O_3	343	20/20	NEt_3	10	30
Au NP/TiO_2	343	20/20	NEt_3	5.5	

Table S4. Comparisons of catalytic activities for the dehydrogenation of formic acid without additives catalyzed by previously reported heterogeneous catalysts with that synthesized in this work.

Catalyst	Temperature /K	$TOF_{Initial}$ /h^{1}	Reference
$PdMn_{0.6}$@S-1	**298**	**610**	**This work**
	333	**6860**	
Au@Schiff-SiO_2	323	4368	31
Pd/mpg-C_3N_4	298	144	24
Au_2Pd_3@(P)N-C	303	358.3	32
CoAuPd/C	298	80	33
Pd/PDA-rGO	323	3505	34
Pd-MnO_x/N-SiO_2	333	2150	35
PdAg-MnO_x/N-SiO_2	323	1430	36
AgPd@NH_2–UiO-66	353	1413	37
AuPd–MnO_x/ZIF-8–rGO	298	409	38
NiPd/**N**H_2-N-rGO	298	954.3	39
Pd_1Au_1/30-LA	333	8355	40
IrPdAu/NH_2-SBA-15	298	4737	41
Au_1Pd_1/NH_2-N-rGO	298	4445.6	42

Table S5. Energies of intermediates and transition states on Pd_{13} and $Pd_8Mn_5O(OH)_{13}$. All energies are with respect to the clean cluster (including spectator O* and OH* species for $Pd_8Mn_5O(OH)_{13}$), CO_2(g), and H_2(g). HCOOH(g) has an energy of –0.14 eV based on this definition. '*' denotes an adsorbed intermediate.

Species	Energies of Species on Clusters / eV	
	Pd_{13}	$Pd_8Mn_5O(OH)_{13}$
Intermediates		
H*	–0.72	–0.32
HCOO*	–1.12	–0.55
HCOOH*	–1.13	–0.77
$HCOO_M$*	–0.34	0.08
Transition State		
H*+H*→H_2(g)	–0.75	–0.11
HCOO*→$HCOO_M$*	–0.20	0.22
$HCOO_M$*→CO_2(g)+H*	–0.31	0.23
HCOOH*→HCOO*+H*	–0.76	–0.71
Coadsorbed Intermediates		
H*+H*	–1.43	–0.97
HCOO*+H*	–1.79	–1.02
$HCOO_M$*+H*	–1.04	–0.41
Coadsorbed Transition States		
HCOO*+H*→$HCOO_M$*+H*	–0.98	–0.25
$HCOO_M$*+H*→CO_2(g)+2H*	–0.91	–0.26

References

(1) Kresse, G. & Furthmüller, J. Efficiency of ab-initio total energy calculations for metals and semiconductors using a plane-wave basis set. *Comput. Mater. Sci.* **1996**, 6, 15–50.

(2) Kresse, G. & Furthmüller, J. Efficient iterative schemes for ab initio total-energy calculations using a plane-wave basis set. *Phys. Rev. B* **1996**, 54, 11169–11186.

(3) Blöchl, P. E. Projector augmented-wave method. *Phys. Rev. B* **1994**, 50, 17953–17979.

(4) Kresse, G. & Joubert, D. From ultrasoft pseudopotentials to the projector augmented-wave method. *Phys. Rev. B* **1999**, 59, 1758–1775.

(5) Erdew, J. P., Burke, K. & Ernzerhof, M. Generalized Gradient Approximation Made Simple. *Phys. Rev. Lett.* **1996**, 77, 3865–3868.

(6) Grimme, S., Antony, J., Ehrlich, S. & Krieg, H. A consistent and accurate ab initio parametrization of density functional dispersion correction (DFT-D) for the 94 elements H-Pu. *J. Chem. Phys.* **2010**, 132, 154104.

(7) Neugebauer, J. & Scheffler, M. Adsorbate-substrate and adsorbate-adsorbate interactions of Na and K adlayers on Al(111). *Phys. Rev. B* **1992**, 46, 16067–16080.

(8) Makov, G. & Payne, M. C. Periodic boundary conditions in ab initio calculations. *Phys. Rev. B* **1995**, 51, 4014–4022.

(9) Henkelman, G., Uberuaga, B. P. & Jonsson, H. A climbing image nudged elastic band method for finding saddle points and minimum energy paths. *J. Chem. Phys.* **2000**, 113, 9901–9904.

(10) Hoover, W. G. Canonical dynamics: Equilibrium phase-space distributions. *Phys. Rev. A* **1985**, 31, 1695–1697.

(11) Nosé, S. A unified formulation of the constant temperature molecular dynamics methods. *J. Chem. Phys.* **1984**, 81, 511–519.

(12) Tang, W., Sanville, E. & Henkelman, G. A grid-based Bader analysis algorithm without lattice bias. *J. Phys. Condens. Matteree.***2009**, 21, 8.

(13) Sanville, E., Kenny, S. D., Smith, R. & Henkelman G. An improved grid-based algorithm for Bader charge allocation. *J. Comp. Chem.* **2007**, 28, 899-908.

(14) Henkelman, G., Arnaldsson, A., & Jónsson, H. A fast and robust algorithm for Bader decomposition of charge density. *Comput. Mater. Sci.* **2006**, 36, 354-360.

(15) Monkhorst, H. J. & Pack, J. D. Special Points for Brillouin-Zone Integrations. *Phys. Rev. B* **1976**, 13, 5188–5192.

(16) Anisimov, V. I., Zaanen, J. & Andersen, O. K. Band theory and Mott insulators: Hubbard U instead of Stoner I. *Phys. Rev. B* **1991**, 44, 943–954.

(17) Jain, A. *et al.* Formation enthalpies by mixing GGA and GGA+U calculations. *Phys. Rev. B* **2011**, 84, 045115.

(18) Ganguly, S., Kabir, M., Autieri, C. & Sanyal, B. Manipulating magnetism of MnO nano-clusters by tuning the stoichiometry and charge state. *J. Phys. Condens. Matter* **2015**, 27, 056002.

(19) Irikura, K. K. Appendix B: Essential Statistical Thermodynamics. in *Computational Thermochemistry: Prediction and Estimation of Molecular Thermodynamics* (eds. Irikura, K. K. & Frurip, D. J.) **1998**, 402–418 (American Chemical Society).

(20) Kim, M. H., Kim, C. S., Lee, H. W. & Kim, K. Temperature dependence of dissociation constants for formic acid and 2,6-dinitrophenol in aqueous solutions up to 175°C. *J. Chem. Soc. Faraday Trans.* **1996**, 92, 4951–4956.

(21) Martínez, J. I. *et al.* Fast prediction of adsorption properties for platinum nanocatalysts with generalized coordination numbers. *Angew. Chem. Int. Ed.* **2014**, 53, 8316–8319.
(22) Zhang, Z., Zhang, L., Hülsey, M. J. & Yan, N. Zirconia phase effect in Pd/ZrO_2 catalyzed CO_2 hydrogenation into formate. *Mol. Catal.* **2019**, 475, 110461.
(23) Liu, Q. *et al.* Direct catalytic hydrogenation of CO2 to formate over a Schiff-base-mediated gold nanocatalyst. *Nat. Commun.* **2017**, 8, 1407.
(24) Lee, J. H. *et al.* Carbon dioxide mediated, reversible chemical hydrogen storage using a Pd nanocatalyst supported on mesoporous graphitic carbon nitride. *J. Mater. Chem. A* **2014**, 2, 9490-9495.
(25) Xu, Z., McNamara, N. D., Neumann, G. T., Schneider, W. F. & Hicks, J. C. Catalytic Hydrogenation of CO_2 to Formic Acid with Silica-Tethered Iridium Catalysts. *ChemCatChem* **2013**, 5, 1769-1771.
(26) Mori, K., Taga, T. & Yamashita, H. Isolated Single-Atomic Ru Catalyst Bound on a Layered Double Hydroxide for Hydrogenation of CO_2 to Formic Acid. *ACS Catal.* **2017**, 7, 3147-3151.
(27) Mori, K., Sano, T., Kobayashi, H. & Yamashita, H. Surface Engineering of a Supported PdAg Catalyst for Hydrogenation of CO_2 to Formic Acid: Elucidating the Active Pd Atoms in Alloy Nanoparticles. *J. Am. Chem. Soc.* **2018**, 140, 8902-8909.
(28) Shao, X. *et al.* Iridium Single-Atom Catalyst Performing a Quasi-homogeneous Hydrogenation Transformation of CO_2 to Formate. *Chem* **2019**, 5, 693-705.
(29) Mori, K. *et al.* Phenylamine-functionalized mesoporous silica supported PdAg nanoparticles: a dual heterogeneous catalyst for formic acid/CO_2-mediated chemical hydrogen delivery/storage. *Chem. Commun.* **2017**, 53, 4677-4680.
(30) Filonenko, G. A., Vrijburg, W. L., Hensen, E. J. M. & Pidko, E. A. On the activity of supported Au catalysts in the liquid phase hydrogenation of CO_2 to formates. *J. Catal.* 343, 97-105 (2016).
(31) Liu, Q. *et al.* A Schiff base modified gold catalyst for green and efficient H2 production from formic acid. *Energ. Environ. Sci.* **2015**, 8, 3204-3207.
(32) Wang, Q. *et al.* Phosphate-Mediated Immobilization of High-Performance AuPd Nanoparticles for Dehydrogenation of Formic Acid at Room Temperature. *Adv. Funct. Mater.* **2019**, 29, 1903341.
(33) Wang, Z. L. *et al.* An Efficient CoAuPd/C Catalyst for Hydrogen Generation from Formic Acid at Room Temperature. *Angew. Chem. Int. Ed.* **2013**, 52, 4406-4409.
(34) Song, F.-Z., Zhu, Q.-L., Tsumori, N. & Xu, Q. Diamine-Alkalized Reduced Graphene Oxide: Immobilization of Sub-2 nm Palladium Nanoparticles and Optimization of Catalytic Activity for Dehydrogenation of Formic Acid. *ACS Catal.* **2015**, 5, 5141-5144.
(35) Bulut, A. *et al.* Pd-MnOx nanoparticles dispersed on amine-grafted silica: Highly efficient nanocatalyst for hydrogen production from additive-free dehydrogenation of formic acid under mild conditions. *Appl. Catal. B-environ* **2015**, 164, 324-333.
(36) Bulut, A. *et al.* MnOx-Promoted PdAg Alloy Nanoparticles for the Additive-Free Dehydrogenation of Formic Acid at Room Temperature. *ACS Catal.* **2015**, 5, 6099-6110.
(37) Gao, S.-T., Liu, W., Feng, C., Shang, N.-Z. & Wang, C. A Ag-Pd alloy supported on an amine-functionalized UiO-66 as an efficient synergetic catalyst for the dehydrogenation of formic acid at room temperature. *Catal. Sci. Technol.* **2016**, 6, *869-874*.
(38) Yan, J.-M. *et al.* AuPd-MnO_x/MOF-Graphene: An Efficient Catalyst for Hydrogen Production from Formic Acid at Room Temperature. *Adv. Energ. Mater.* **2015**, 5, 1500107.
(39) Yan, J.-M. *et al.* Anchoring and Upgrading Ultrafine NiPd on Room-Temperature-Synthesized

Bifunctional NH_2-N-rGO toward Low-Cost and Highly Efficient Catalysts for Selective Formic Acid Dehydrogenation. *Adv. Mater.* **2018**, 30, 1703038.
(40) Hong, W. *et al.* Immobilization of highly active bimetallic PdAu nanoparticles onto nanocarbons for dehydrogenation of formic acid. *J. Mater. Chem. A* **2019**, 7, 18835-18839.
(41) Luo, Y. et al. Anchoring IrPdAu Nanoparticles on NH2-SBA-15 for Fast Hydrogen Production from Formic Acid at Room Temperature. *ACS Appl. Mater. Interfaces* **2020**, 12, 8082−8090.
(42) Li, S. et al. A Simple and Effective Principle for a Rational Design of Heterogeneous Catalysts for Dehydrogenation of Formic Acid. *Adv. Mater.* **2019**, 31, 1806781.